pharmaceutics

MDPI

Review

Targeted Radiopharmaceuticals for Synovitis: Emerging Molecular Imaging and Theranostic Perspectives

Myrna Luna-Gutiérrez [1], Blanca Ocampo-García [1], Erika Azorín-Vega [1], Laura Meléndez-Alafort [2,*] and Guillermina Ferro-Flores [1,*]

[1] Department of Radioactive Materials, Instituto Nacional de Investigaciones Nucleares, Ocoyoacac 52750, Mexico
[2] Immunology and Molecular Oncology Diagnostics Unit, Veneto Institute of Oncology IOV-IRCCS, 35128 Padua, Italy
* Correspondence: laura.melendezalafort@iov.veneto.it (L.M.-A.); guillermina.ferro@inin.gob.mx (G.F.-F.)

Abstract

The management of rheumatoid arthritis and related inflammatory arthropathies is evolving from late structural assessment toward early molecular phenotyping of synovitis. Target-specific radiopharmaceuticals for positron emission tomography (PET) and single-photon emission computed tomography (SPECT) now permit non-invasive detection of activated fibroblast-like synoviocytes, inflammatory macrophages, chemokine-driven immune-cell trafficking, angiogenesis, and mitochondrial stromal activation. This review analyzes the radiochemical basis of synovitis imaging, beginning with the radionuclide-dependent behavior of ^{11}C, ^{68}Ga, ^{64}Cu, [Al^{18}F]$^{2+}$, and ^{99m}Tc, and then linking these properties to chelator selection, covalent radiolabeling, labeling conditions, and pharmacokinetics. The review further examines the development of radioligands targeting fibroblast activation protein (FAP), integrin $\alpha_v\beta_3$, folate receptor beta (β-FR), CXCR4, and the 18 kDa translocator protein (TSPO). It covers FAP-inhibitor scaffolds, RGD-based integrin probes, pteroyl-glutamate folate conjugates, CXCR4 antagonists, and TSPO heteroaromatic ligands. Clinical and translational datasets are discussed in relation to disease-activity evolution, treatment-response monitoring, and differentiation of stromal activation, macrophage infiltration, angiogenesis, and immune-cell recruitment. Finally, the review integrates kinetic modeling and dosimetric translation, emphasizing absorbed-dose estimation as a perspective on therapeutic optimization and safety constraints for emerging β-emitting and α-emitting synovial theranostics, ^{177}Lu and ^{225}Ac. Collectively, these developments define a bench-to-bedside framework for rheumatology precision medicine, in which radiopharmaceutical chemistry, molecular imaging, clinical trial evidence, and patient-specific dosimetry converge to guide diagnosis, therapeutic selection, and future targeted synovial micro-radioresection.

Keywords: rheumatoid arthritis; synovitis; radiopharmaceuticals; PET/SPECT imaging; targeted synovial theranostics

Check for updates

Academic Editor: Frank Wuest

Received: 27 August 2026
Revised: 22 October 2026
Accepted: 24 October 2026
Published: 1 November 2026

Copyright: © 2026 by the authors. Licensee MDPI, Basel, Switzerland. This article is an open access article distributed under the terms and conditions of the Creative Commons Attribution (CC BY) license.

1. Introduction

Rheumatoid arthritis (RA) and related chronic inflammatory arthropathies represent a massive global socioeconomic burden, characterized by persistent synovial inflammation, progressive articular destruction, and severe systemic comorbidities [1]. For decades, the clinical management of these autoimmune diseases has relied on therapeutic interventions initiated after macrostructural bone erosions or joint narrowing became visible on conventional radiography [2]. While the clinical introduction of biological and targeted

synthetic disease-modifying antirheumatic drugs (DMARDs), such as anti-TNF agents and JAK inhibitors, has revolutionized patient outcomes, a major clinical problem remains: a significant cohort of patients fails to achieve sustained clinical remission due to delayed diagnosis or non-responsive therapeutic stratification [3]. Consequently, modern rheumatology is undergoing a critical shift toward precision medicine, aiming to detect subclinical synovial alterations and predict individual therapeutic responses at the molecular level before anatomical damage becomes irreversible [4–6].

Conventional diagnostic modalities, including contrast-enhanced magnetic resonance imaging (MRI) and musculoskeletal ultrasound (MSUS), offer high soft-tissue contrast but inherently lack the biochemical specificity required to differentiate active cellular proliferation from passive tissue remodeling or resolving inflammation [7]. Similarly, the traditional nuclear medicine standard, ^{18}F-FDG PET, is severely limited in rheumatology due to its nonspecific uptake in any high-glucose-metabolizing tissue, frequently leading to false-positive signals from physiological muscular exertion or osteoarthritis [8]. To overcome these diagnostic ambiguities, target-specific radiopharmaceuticals are being developed to map the hyperactive cellular phenotypes that drive synovial inflammation. Within the inflamed synovial microenvironment, the key pathological driver is the transformation of quiescent cells into aggressive phenotypes. The most relevant of these are activated fibroblast-like synoviocytes (FLSs) and pro-inflammatory M1-like synovial macrophages, which collectively secrete the proteolytic enzymes and cytokines responsible for cartilage degradation [4,5,9,10]. Nuclear medicine now offers target-specific tools for molecular phenotyping of synovitis by exploiting the distinct molecular signatures of activated synovial fibroblasts, inflammatory macrophages, chemokine-driven immune-cell populations, and angiogenic endothelium. The scope of this review is to provide an integrated review of positron emission tomography (PET) and single-photon emission computed tomography (SPECT) radiopharmaceuticals for rheumatoid arthritis and related inflammatory arthropathies, beginning with the chemical and coordination features of the involved radionuclides and radionuclide possible strategies (^{11}C, ^{68}Ga, ^{64}Cu, [Al^{18}F]$^{2+}$, and ^{99m}Tc) and then relating these properties to chelator selection, covalent radiolabeling, radiolabeling conditions, pharmacokinetics, and image contrast. Although ^{11}C is not a coordination radionuclide, its 20.4 min half-life and ability to label small organic 18 kDa translocator protein (TSPO) ligands without substantially altering pharmacophore structure make it central to macrophage/stromal activation imaging, especially for [^{11}C]PK11195, [^{11}C]PBR28, and [^{11}C]DPA-713 [11–13]. Particular emphasis is placed on radioligands directed against fibroblast activation protein (FAP), integrin $\alpha_v\beta_3$, folate receptor beta (β-FR), C-X-C chemokine receptor type 4 (CXCR4), and TSPO, all of them molecular targets and biomarkers of the inflamed synovium because each identifies a distinct pathogenic niche within the rheumatoid pannus (Figure 1). FAP marks activated fibroblast-like synoviocytes and fibroblast-driven matrix remodeling; integrin $\alpha_v\beta_3$ reflects angiogenic endothelium and matrix-adhesive vascular expansion; β-FR identifies activated macrophage-rich inflammatory infiltrates; CXCR4 reports chemokine-mediated recruitment and retention of inflammatory immune cells; and TSPO captures mitochondrial activation in macrophages, fibroblast-like synoviocytes, and other metabolically active inflammatory cells (Figure 1) [4,5,9,10]. Therefore, fibroblast activation protein inhibitors (FAPIs), arginine-glycine-aspartate (RGD)-based integrin probes, folate conjugates, CXCR4 ligands, and TSPO heteroaromatic tracers were included. The review further evaluates clinical and translational evidence for disease-activity evolution, treatment-response monitoring, and molecular pathotyping, before integrating prospective kinetic modeling and dosimetry, and possible safety constraints for emerging β-emitting (^{177}Lu) and α-emitting (^{225}Ac) synovial theranostic strategies. In this way, the review connects radiopharmaceutical chemistry, molecular imaging performance, clinical

trial evidence, and targeted synovial micro-radioresection into a coherent bench-to-bedside framework for rheumatology precision medicine.

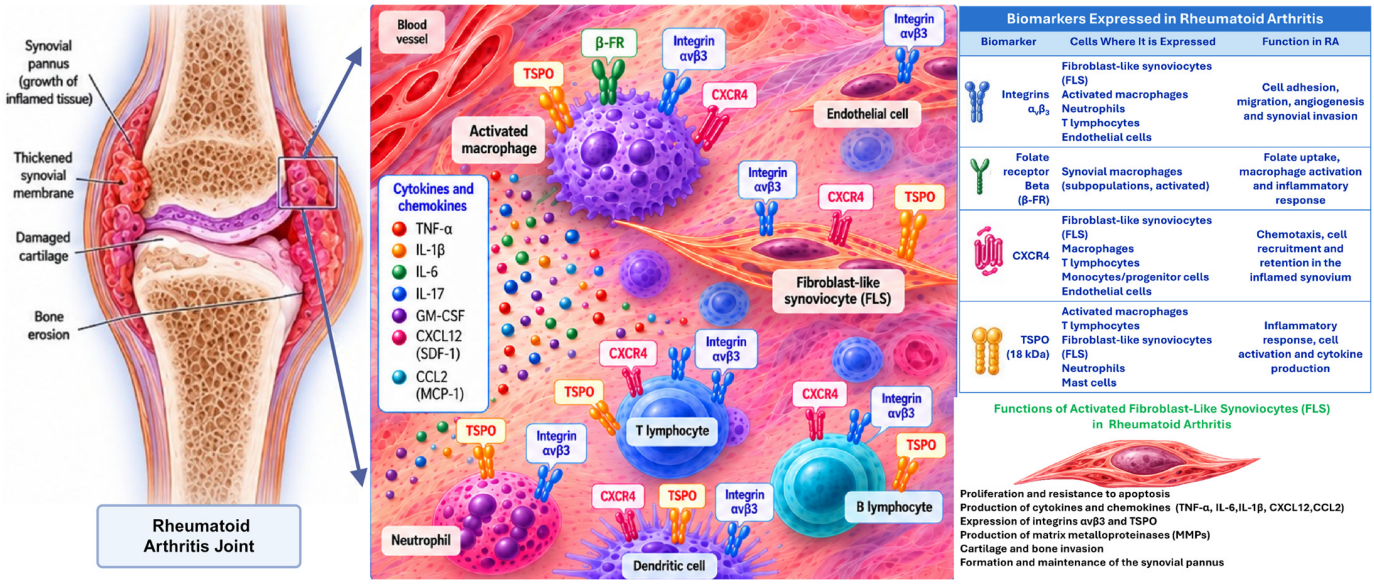


Figure 1. Molecular biomarker environment of the inflamed rheumatoid synovium. The schematic summarizes the targets discussed in this review: FAP-positive activated fibroblast-like synoviocytes involved in matrix remodeling and pannus invasion; integrin $\alpha_v\beta_3$-expressing angiogenic endothelium supporting neovascular expansion; β-FR-positive activated macrophages reflecting macrophage-rich inflammatory burden; CXCR4-positive immune-cell populations mediating chemokine-driven recruitment and retention; and TSPO-expressing metabolically activated macrophages, fibroblast-like synoviocytes, and stromal inflammatory cells. Together, these targets provide complementary PET/SPECT imaging readouts for molecular phenotyping, disease activity assessment, therapeutic response monitoring, and future synovial theranostic stratification in rheumatoid arthritis and related inflammatory arthropathies [4,5,9,10]. (Created in BioRender. Ocampo, B. (2026) https://BioRender.com/gprajoy).

2. Chemical and Coordination Aspects of Radionuclides

2.1. Radiometal Coordination and Radiofluorination Principles

The first important topic is the radionuclide or labeling strategy itself, because half-life, emission properties, oxidation state, coordination geometry, and radiochemical route determine whether a tracer is best suited for PET, SPECT, delayed imaging, or therapeutic translation. ^{11}C, ^{68}Ga, ^{64}Cu, $[Al^{18}F]^{2+}$, and ^{99m}Tc therefore define the chemical boundary conditions for synovial radioligand design. For radiometals and $[Al^{18}F]^{2+}$, performance is governed mainly by donor-atom preference and coordination stability; for ^{11}C, the defining constraints are covalent incorporation, rapid radiosynthesis, on-site cyclotron production, and short imaging windows [11–19].

In synovitis-targeted radiopharmaceuticals, chelator, linker, and prosthetic-group engineering must match both the biological target and the recognition element. Radiolabeling of ligands targeting FAP, CXCR4, β-FR, integrin $\alpha_v\beta_3$, or TSPO must preserve receptor or enzyme recognition while minimizing nonspecific retention in blood, liver, muscle, kidney, and periarticular soft tissue. The chelator is therefore not an inert terminal label: its charge, hydrophilicity, steric bulk, and coordination stability can modify affinity, serum stability, clearance pathway, and image contrast [14–23]. PET agents must keep the binding motif accessible after conjugation to DOTA, NOTA, NODAGA, RESCA, SarAr, TETA, CB-TE2A, or $[Al^{18}F]^{2+}$-compatible chelators. In contrast, SPECT agents based on HYNIC or tricarbonyl ^{99m}Tc chemistry depend on the coordination co-ligands, linker, and targeting motif to deter-

mine radiochemical purity, in vivo stability, elimination pathway, and target-to-background ratio [14–26]. Thus, ^{68}Ga, ^{64}Cu, and reduced ^{99m}Tc cores undergo direct coordination within a ligand cavity, whereas $[Al^{18}F]^{2+}$ acts as a pre-assembled pseudo-radiometal cation that requires a specialized macrocyclic or restrained framework to preserve the Al-F bond, in which ^{18}F is retained through a polarized Al-F bond while Al^{3+} occupies the chelator cavity [14–19]. The structure–performance framework is the key for translating synovitis ligands across PET, SPECT, and future theranostic applications.

2.2. *^{68}Ga and ^{64}Cu Coordination Characteristics*

Gallium-68 ($t_{1/2}$ = 1.13 h; β^+: E_{max} 1899 keV, 87.7%), generally obtained from a ^{68}Ge/^{68}Ga generator, is a hard, high-charge-density d^{10} trivalent cation that lacks crystal-field stabilization energy; therefore, its preferred geometry is mainly influenced by ionic radius, steric fit, and electrostatic interactions. It favors an octahedral coordination sphere with hard donors such as oxygen and nitrogen. NOTA and NODAGA are particularly well matched to Ga^{3+} because its smaller nine-membered ring efficiently satisfies the hexacoordinate environment at mild conditions. In contrast, DOTA generally requires higher temperatures to overcome conformational barriers before forming a kinetically inert Ga-DOTA complex [14,15,27,28]. Nevertheless, [^{68}Ga]Ga-DOTA-ligand complexes can shift biodistribution toward rapid renal excretion, reduce nonspecific periarticular retention, and improve the target-to-background ratios required to detect upregulated proteins during early rheumatoid arthritis; as relevant, they can be used as theranostic pairs with ^{177}Lu or even ^{225}Ac.

Copper-64 ($t_{1/2}$ = 12.7 h; β^+: 17.5%; β^-: 38.5%) has a decay profile that enables ^{64}Cu-based radiopharmaceuticals to be used for PET imaging and radionuclide therapy. The combination of β^+ emissions (maximum energy 652.6 keV; 17.5%) and β^- emissions (maximum energy 579 keV; 38.5%) delivers a high local radiation dose at the cellular level. Furthermore, electron capture decay (43.5%) is accompanied by the emission of Auger electrons, which also contributes to its cytotoxic potency. The longer half-life of ^{64}Cu compared to ^{68}Ga potentially enables delayed pannus synovium imaging, allowing the radiopharmaceutical to clear from healthy tissues and improve the target-to-background ratios required to detect upregulated proteins involved in the early synovitis process, where the radiopharmaceutical is designed to be retained by a specific molecular recognition mechanism. Additionally, ^{64}Cu has a lower positron energy (E_{max} = 652.6 keV, 17.5%) than ^{68}Ga (E_{max} = 1899 keV, 87.7%), resulting in a shorter mean positron range (0.56 mm versus 3.5 mm). This shorter range is only one contributor to image resolution; practical small-joint accuracy also depends on scanner resolution, reconstruction, count statistics, motion, and partial-volume effects [14,16,17].

Cu(II) has a d^9 electronic configuration and commonly exhibits Jahn–Teller distortion, which produces elongated axial bonds and flexible coordination numbers of four, five, or six. Because Cu^{2+} has borderline hard-soft behavior, it interacts favorably with nitrogen-rich macrocycles and selected sulfur donors. These properties make copper chemically stable for delayed PET imaging but also increase the risk of in vivo transchelation when the coordination cage is not sufficiently rigid [14,16,17]. To reduce dissociation and biological capture by endogenous proteins such as superoxide dismutase, ^{64}Cu radiopharmaceuticals frequently employ SarAr, TETA, NOTA, NODAGA, and cross-bridged CB-TE2A-type frameworks, which provide enhanced cage-like confinement for the radionuclide. These chelators bind Cu^{2+} within a more rigid or better-matched coordination cavity, enhancing kinetic inertness, reducing nonspecific hepatic background, and prolonging blood-pool clearance intervals, which are useful for delayed imaging strategies in small joints [16,17,29]. However, DOTA is also frequently used as a copper chelator because, as in the case of ^{68}Ga, [^{64}Cu]Cu-DOTA complexes can act as theranostic pairs with the therapeutic radionuclides ^{177}Lu and ^{225}Ac [29].

2.3. ^{99m}Tc Coordination Features

Technetium-99m ($t_{1/2}$ = 6 h; γ 140.5 keV, 88.5%) differs from gallium and copper because it is obtained from ^{99}Mo/^{99m}Tc generators as pertechnetate ($[TcO_4]^-$, Tc(VII)) and must be reduced, commonly with $SnCl_2$, to generate lower-valent coordination cores suitable for radiopharmaceutical labeling. Depending on precursor chemistry, ^{99m}Tc is most frequently incorporated via the oxo, diazenido, HYNIC, tricarbonyl, or mercaptoacetyltriglycine (MAG) strategies. The tricarbonyl approach uses the organometallic fac-$[^{99m}Tc(CO)_3]^+$ core, which is well suited for ligands bearing histidine, imidazole, iminodiacetic acid, or other tridentate N/O/S donor sets, whereas MAG3 labeling exploits an N_3S tetradentate chelation motif to stabilize Tc(V) oxo complexes and enable peptide or small-molecule conjugation [18]. In HYNIC-based systems, co-ligands such as tricine and EDDA complete the coordination sphere and modulate hydrophilicity, charge, and biological clearance [24]. Recent publications of ^{99m}Tc-labeled targeting vectors in RA further support SPECT/CT as a practical molecular-imaging route when PET access is limited [18,24,30]. Ali et al. emphasize that ^{99m}Tc-labeled targeting vectors can be adapted to macrophage-, folate-, peptide-, or receptor-directed designs and translated through generator availability, kit-like preparation, and SPECT/CT infrastructure already present in many nuclear medicine departments [30].

2.4. $[Al^{18}F]^{2+}$ Coordination Characteristics

Aluminum fluoride labeling occupies a distinct position between conventional radiohalogenation and radiometal coordination. In this strategy, cyclotron-produced $^{18}F^-$ is first combined with Al^{3+} to form the cationic $[Al^{18}F]^{2+}$ species, which is then captured by a suitable chelator attached to the biological vector. The resulting construct behaves as a pseudo-radiometal complex: fluorine-18 provides the favorable PET properties of high positron yield, low positron energy, and a 109.8 min half-life, whereas aluminum enables the label to be introduced via aqueous chelation chemistry rather than multi-step covalent radiofluorination [19,27,31,32]. Aluminum is a hard trivalent center with a strong preference for oxygen and nitrogen donor atoms, and the Al-F bond must remain protected inside a compact chelator cavity. NOTA and NODA-derived systems stabilize the complex efficiently but often require heating, which may limit use with thermolabile peptides, proteins, or fragile multivalent constructs. Restrained complexing agents such as RESCA were developed to reduce this thermal burden and enable $Al^{18}F$ labeling under milder conditions, including room-temperature protocols in appropriate biomolecular platforms [19,31].

For synovitis-targeted radiopharmaceuticals, this chemistry is especially relevant because it combines the logistical scalability of fluorine-18 ($t_{1/2}$ = 1.8 h; β^+: Emax 633.5 keV, 96.7%) with the modularity of chelator-bearing FAP, CXCR4, folate, and peptide ligands. As with ^{64}Cu, the use of ^{18}F ligands can improve small-joint visualization by leveraging the shorter positron range of fluorine-18 compared with ^{68}Ga, while preserving a kit-like or semi-kit radiochemical workflow compatible with centralized production and distribution [16,19,23,27,31–33]. As ^{18}F is produced from cyclotrons, ^{64}Cu offers logistical advantages over ^{18}F due to its longer half-life, allowing PET scans to be performed at hospitals without a cyclotron.

2.5. ^{11}C Covalent Labeling Features

Carbon-11 ($t_{1/2}$ = 20.4 min; β^+: Emax 960 keV, 99.8%) is chemically distinct from the radiometal and $[Al^{18}F]^{2+}$ systems because it is incorporated covalently into small organic molecules rather than coordinated by a chelator. Its short half-life enables same-day serial PET studies. It minimizes the residual radiation burden but also requires an on-site cyclotron, rapid synthesis, fast purification, and immediate quality control. These

features make ^{11}C especially suitable for lipophilic heteroaromatic TSPO ligands such as [^{11}C]PK11195, [^{11}C]PBR28, and [^{11}C]DPA-713, where preserving the native pharmacophore is essential for receptor binding and kinetic interpretation [11–13].

2.6. Summarizing: Radionuclide Selection

The choice among ^{11}C, ^{68}Ga, ^{18}F, and ^{64}Cu-labeled PET radiopharmaceuticals represents a critical axis in chemical synthesis, directly impacting spatial resolution, imaging logistics, and clinical scalability. Although ^{68}Ga remains a historical standard for FAPI imaging due to generator-based availability, its higher positron energy produces a longer mean range in tissue, which can blur small hand and foot joints where precise quantification of synovial inflammation is crucial: ^{18}F and ^{64}Cu offer lower positron energy, shorter range, and sharper spatial resolution. In contrast, ^{11}C is best suited to short-window receptor probes, especially TSPO tracers, because covalent labeling can preserve the parent ligand structure but requires tightly integrated cyclotron–radiochemistry–PET workflows [11–13].

Furthermore, ^{64}Cu has a longer half-life of 12.7 h, which supports delayed imaging. Unlike ^{68}Ga and ^{18}F, which are commonly imaged within the first hours after injection, ^{64}Cu-radiotracers can support delayed PET acquisition at later time points when the biological vector and chelator remain stable [14,16,17,27–29,33].In RA, this capability should be interpreted as a radiochemical and logistical advantage.

To engineer the optimal targeted diagnostic radiopharmaceutical for synovitis, medicinal chemists must balance different thermodynamic, kinetic, and coordination behaviors across both PET and SPECT modalities. The electronic and structural differences in radionuclide-ligand complexes directly affect the tracer's core stability, lipophilicity, and diagnostic imaging window, as shown in Table 1.

Table 1. Thermodynamic, Kinetic, and Physicochemical Comparison of PET and SPECT Isotopic Cores in Targeted Radiopharmaceuticals.

Radiochemical Parameter [Ref.]	**Gallium-68 ($^{68}Ga^{3+}$) [PET]**	**Copper-64 ($^{64}Cu^{2+}$) [PET]**	**Aluminum Fluoride ($[Al^{18}F]^{2+}$) [PET]**	**Technetium-99m Core ($[Tc{=}O]^{3+}$/$[Tc(CO)_3]^{+}$) [SPECT]**
Coordination Geometry [14–19,27–29,33]	Octahedral (Hexacoordinate)	Tetragonally distorted octahedral/Square pyramidal	Pentadentate or Hexadentate envelope	Pseudo-octahedral (Tricarbonyl)/Distorted square pyramidal (HYNIC)
Preferred Donor Atoms [14–19,27–29,33]	Hard oxygen and nitrogen (N_3O_3)	Borderline nitrogen and sulfur (N_4, N_2S_2)	Mixed hard oxygen, nitrogen, and halides	Tricarbonyl: Facial tridentate N/O/S donors HYNIC: Mixed N-donors with tricine/EDDA
Optimal Chelators [14–19,27–29,33]	NOTA, NODAGA, DOTA	NOTA, NODAGA, SarAr, TETA, Cross-bridged CB-TE2A	NOTA, NODA derivatives, RESCA (Restrained complexing agent)	Tricarbonyl: Histidines/Iminodiacetic acid, HYNIC: 6-Hydrazinonicotinamide
Thermodynamic Stability (log K_{ML} [14–19,27–29,33]	High (~21.0–31.0 with NOTA/DOTA)	Very high (~22.0–25.0 with specialized cages)	High conditional stability in aqueous systems	High; controlled by the kinetic inertness of the $[^{99m}Tc(CO)_3]^{+}$ core or co-ligand ratios
Kinetic Inertness [14–19,27–29,33]	High at physiological pH	High only when using rigid polyamine macrocyclic cages	Extremely high; prevents in vivo defluorination	High for tricarbonyl complexes; high for HYNIC with EDDA/tricine co-ligands
Physical Half-Life ($t_{1/2}$) [11–19,27–29,33]	68 min	12.7 h	110 min	6.0 h
Primary Emission & Energy [11–19,30]	Positron ($E_{\beta+max}$ = 1.89 MeV)	Positron ($E_{\beta+max}$ = 0.65 MeV)	Positron ($E_{\beta+max}$ = 0.63 MeV)	Gamma (γ) photon: 140 keV (No tissue-range blurring; limits determined by collimator geometry)
Labeling Conditions [11–19,23–29,31–33]	25–95 °C, pH 3.5–4.5	25–95 °C, pH 5.5–6.5	100–120 °C, pH 4.0–5.0	95 °C (Kit-based reduction), pH 5–7

3. Design of Synovial-Targeted Radioligands

After establishing the radionuclide coordination framework, the next step is to design radioligands that target disease-driving molecular targets in synovitis. Each target requires a different recognition element: quinoline-based inhibitors for FAP, RGD-based peptides for integrin $\alpha_v\beta_3$, pteroyl-glutamate conjugates for β-FR, heteroaromatic ligands for TSPO, and CXCR4-binding cyclic peptides or antagonists. These recognition elements are then coupled to bifunctional chelators or prosthetic groups according to the coordination requirements described above, linking chemical architecture directly to biological performance.

3.1. Fibroblast Activation Protein Inhibitors

Fibroblast activation protein (FAP) is an integral membrane enzyme with dipeptidyl peptidase and endopeptidase activity. The most successful radiotracers, such as FAPI derivatives, are competitive enzymatic inhibitors with picomolar or low-nanomolar affinity [34]. The catalytic pocket of FAP traps the inhibitor through coordination bonds and van der Waals and hydrophobic interactions, so tight and rigid that the dissociation constant (k_{off}) is negligible in the short and medium term. Although the bond is not always formally covalent and therefore chemically reversible, it behaves biokinetically as quasi-reversible trapping because the tracer retention time in the target greatly exceeds the blood clearance rate, preventing the tracer from re-equilibrating with blood plasma during data acquisition [34,35].

FAP is highly expressed by activated fibroblast-like synoviocytes (FLS) in the rheumatoid pannus, where it plays a critical role in fibroblast proliferation, migration, extracellular-matrix remodeling, inflammatory cross-talk, angiogenesis, and cartilage invasion [20–26]. Current reports on FAP-targeted (FAPI) radiopharmaceuticals encompass a comprehensive range of evidence, including direct rheumatoid arthritis (RA) imaging studies, pharmacokinetic optimization, SPECT/PET probe development, fibroinflammatory pathology reviews, and extensive oncology-derived theranostic data [20–26,36–41]. To ensure clinical accuracy, specific knowledge about RA, including diagnostic performance, treatment monitoring, and disease staging, should ideally be based on data from RA patient cohorts. Meanwhile, scientific reports focused on clinical chemistry provide the necessary foundation for design principles, radiolabeling strategies, pharmacokinetics, and translational feasibility [20–26,36–41].

From a medicinal chemistry perspective, the canonical PET FAPI platform features a FAP-binding pharmacophore composed of a quinoline or quinolinoyl recognition unit linked to a glycyl-2-cyanopyrrolidine; the cyanopyrrolidine moiety directly engages the catalytic pocket, while the quinoline scaffold and its adjacent linker modulate selectivity, internalization kinetics, plasma clearance, and background retention. Well-established diagnostic PET derivatives, such as FAPI-04 and FAPI-46, are routinely conjugated to chelating systems, including DOTA, NOTA, NODAGA, RESCA, SarAr, and TETA, which allows this versatile receptor-binding scaffold to accommodate various radionuclides like ^{68}Ga, ^{18}F-AlF, ^{64}Cu, or therapeutic radiometals, while maintaining structural hydrophilicity and favoring renal excretion. A central focus in designing these agents is optimizing the spatial separation between the FAP-binding warhead and the bulky coordination core, as managing linker length, charge, and lipophilicity is essential to maximize target accessibility, minimize hepatobiliary retention, and reduce nonspecific periarticular signal [20–26,38–41].

To expand imaging accessibility via ^{99m}Tc SPECT, alternative configurations, such as HYNIC-iFAP, have been developed. This platform integrates a boronic-acid FAP-inhibitory motif with a HYNIC-based coordination strategy, using co-ligands such as EDDA or tricine to complete the ^{99m}Tc coordination sphere and facilitate efficient, kit-like radiolabeling with high radiochemical purity and rapid renal elimination [24]. In this context, HYNIC-FAPIs have also been developed [25,26]. Consequently, FAP-targeted radioligands represent a

robust molecular bridge connecting synovial fibroblast biology, coordination chemistry, and quantitative nuclear imaging. At the same time, FAP-directed radionuclide therapy in RA continues to evolve as a promising investigational concept.

3.2. Integrin $\alpha_v\beta_3$

Integrin $\alpha_v\beta_3$, also known as the vitronectin receptor, is a cell-surface receptor protein that links cells to the extracellular matrix and supports cell communication, adhesion, migration, survival, and angiogenesis, including new blood vessel formation during wound healing. At the molecular level, binding of the RGD motif (arginine-glycine-aspartate) to the hydrophilic pocket located between the α_v and β_3 subunits, coordinated by a magnesium or manganese ion at the metal ion-dependent adhesion site, is high-affinity but thermodynamically reversible [42]. Therefore, the radiotracer continuously binds and unbinds with moderate dissociation kinetics (k_{off}). Although integrin $\alpha_v\beta_3$ may undergo clathrin-dependent or clathrin-independent endocytosis during cell migration and angiogenesis, the receptor is not massively degraded in lysosomes but instead follows fast or slow recycling pathways back to the plasma membrane, allowing the dissociated or exocytosed radiotracer to return to the interstitial space and plasma while maintaining a dynamic equilibrium quantifiable through the distribution volume (V_T) [43,44].

Integrin $\alpha_v\beta_3$ is highly expressed in specific synovial cell populations involved in cell migration, extracellular matrix adhesion, and pannus vascularization. Within the pathophysiology of rheumatoid arthritis (RA), neovascular expansion represents a structural requirement for persistent leukocyte influx, synovial hyperplasia, oxygen and nutrient delivery, and progressive cartilage invasion. Consequently, $\alpha_v\beta_3$-targeted imaging provides complementary information to other biomarkers, such as FAP, B-FR, TSPO, and CXCR4, by directly characterizing the angiogenic and matrix-adhesive components of the inflammatory lesion [45–48]. The radiopharmaceutical design of integrin-targeted tracers centers on the canonical RGD recognition sequence, which mimics extracellular matrix-binding motifs to interact with the ligand-binding cleft of $\alpha_v\beta_3$. Cyclization of the RGD peptide is commonly utilized to stabilize its bioactive conformation, enhance proteolytic resistance, and increase receptor selectivity.

In contrast, multimerization or dimeric RGD constructs are employed to amplify apparent affinity through avidity effects [34–38]. From a coordination chemistry perspective, these peptide platforms are highly compatible with bifunctional chelators, such as DOTA, NOTA, and NODAGA, for labeling with ^{68}Ga or ^{64}Cu radionuclides, as well as with prosthetic radiofluorination strategies including [^{18}F]Galacto-RGD, [^{18}F]Fluciclatide, and Al^{18}F/NODAGA-RGD complexes [45,49–51]. To optimize pharmacokinetics for small-joint imaging, modifications such as glycosylation, PEGylation, or the introduction of carbohydrate-functionalized linkers are routinely integrated to reduce lipophilicity, shift clearance toward renal elimination, and lower background signal in muscular and hepatic tissues [45,49–52]. In clinical research, [^{68}Ga]Ga-PRGD$_2$ PET/CT has demonstrated specific accumulation in actively inflamed RA synovium characterized by dense neovasculature and elevated $\alpha_v\beta_3$ expression; notably, longitudinal changes in tracer uptake following treatment correlate closely with clinical disease activity, offering a distinct advantage over conventional [^{18}F]FDG in scenarios where FDG signals are confounded by muscular activity or nonspecific metabolic inflammation [47,48]. These studies established $\alpha_v\beta_3$ radioligands as functional biomarkers of angiogenesis rather than general probes of inflammation. Within the broader framework of molecular imaging in RA, integrin-targeted imaging serves as an orthogonal axis of vascular remodeling; it complements rather than replaces FAP imaging of activated fibroblast-like synoviocytes or B-FR/TSPO imaging of inflammatory macrophages, providing a specialized metric of synovial angiogenesis, endothelial activation, and matrix-dependent pannus expansion.

3.3. Folate Receptor-Beta (β-FR)

β-FR is a glycosylphosphatidylinositol (GPI)-anchored protein located on the plasma membrane and is mainly expressed in activated myeloid-lineage macrophages (M2) in tumors and inflammatory settings. Although folates and their conjugates are internalized through receptor-mediated endocytosis, the biological pathway of the folate receptor is structurally designed for rapid recycling. Once the endosome acidifies, the pH change markedly reduces the affinity of β-FR for its ligand, leading to ligand release within the endosome. However, unlike trapping models, the empty β-FR receptor and a substantial fraction of the unmodified ligand recycle back to the cell surface in very short cycles, approximately every 10 to 20 min. This continuous bidirectional flow of internalization, externalization, and dissociation prevents definitive tracer sequestration and generates a continuous dynamic equilibrium with the extracellular free compartment, requiring the system to be modeled according to principles of reversible biokinetics [21,53,54].

β-FR is selectively enriched on activated macrophages within rheumatoid synovium, making it a valuable imaging target for macrophage-dominant synovitis. Folate-based radiopharmaceuticals exploit the high-affinity interaction between the pteroyl-glutamate pharmacophore and folate receptors. At the same time, structural modification of the γ-carboxylate region, spacer length, PEGylation, and chelator attachment enables radiolabeling without disrupting receptor recognition [55–60].

From a molecular-design perspective, the pteroyl core must remain available for receptor binding, whereas the glutamate tail provides a chemically permissive site for linker and chelator conjugation. Hydrophilic PEG or amino-acid linkers are commonly introduced to reduce nonspecific plasma-protein binding, improve renal clearance, and lower periarticular background. This design logic is exemplified by [^{18}F]fluoro-PEG-folate, which demonstrated rapid blood clearance, low background uptake, and favorable target-to-background ratios in RA patients, and by [^{68}Ga]Ga-NOTA-folate, which showed nanomolar B-FR affinity and macrophage-associated inflammatory uptake in preclinical models [56,57].

For SPECT translation, [^{99m}Tc]Tc-EC20/FolateScan, a peptide derived from folic acid consisting of the linear sequence folic acid-pteroic acid (Pte)-D-Glu-β-L-diaminopropionic acid (βDpr)-Asp-Cys, established the clinical feasibility of folate-targeted imaging in RA, detecting active joint involvement and supporting β-FR uptake as a surrogate of activated macrophage burden [60]. However, folate receptor expression in kidneys and physiological handling of folate analogs impose an important pharmacokinetic constraint: renal uptake can be substantial, requiring careful optimization of linker hydrophilicity, injected mass, clearance kinetics, and imaging timing. Therefore, β-FR radioligands are best interpreted as macrophage-targeted inflammation probes whose clinical value depends on achieving high synovium-to-background contrast while limiting renal and systemic retention [55–60].

3.4. 18 kDa Translocating Protein (TSPO)

TSPO is a hydrophobic protein located in the outer mitochondrial membrane and is highly expressed during inflammatory processes. It is composed of five transmembrane helices that form a ligand-binding channel for compounds such as PK11195 or advanced-generation ligands [61–63]. Because TSPO is located in the mitochondria, lipophilic ligands must cross the cell membrane by passive diffusion and bind transiently to the allosteric site or binding pocket of TSPO. There is no endosomal internalization mechanism, nor are covalent bonds formed. The exchange kinetics (k_{on} and k_{off}) are very rapid and balanced. The radioligand continuously binds to and dissociates from the mitochondria, returning to the cytosol and then to the extracellular space [61–65].

Therefore, TSPO is highly upregulated on the outer mitochondrial membrane of both activated macrophages and fibroblast-like synoviocytes (FLSs) within rheumatoid tissues.

Chemically, TSPO ligands exhibit notable structural diversity, encompassing classic benzodiazepines, isoquinoline carboxamides, phenoxyarylacetamides, pyrazolopyrimidines, and various other heteroaromatic scaffolds [11–13,63,65–68]. Early imaging efforts utilized first-generation radioligands such as [^{11}C]PK11195; however, these initial platforms often faced pharmacokinetic challenges, including high lipophilicity, modest signal-to-noise ratios, and substantial nonspecific binding to plasma proteins and healthy tissues, which limited the target-to-background ratio in small peripheral joints [12,13]. To address these limitations, second-generation tracers, including [^{11}C]PBR28, [^{11}C]DPA-713, [^{18}F]GE-180, [^{18}F]FEBMP, and [^{18}F]DPA-714, were developed, successfully enhancing binding affinity, reducing background activity, and improving quantification reliability in inflammatory PET imaging [63,65–69]. In the context of rheumatoid arthritis (RA), TSPO PET signals are best understood as a composite marker rather than a single-cell lineage indicator. Synovial autoradiography and immunostaining demonstrate that TSPO expression is shared among macrophages, FLSs, and selected lymphocyte populations, meaning that TSPO imaging reflects a collective mitochondrial activation signature of the inflammatory pannus. Clinical proof-of-concept studies have validated the ability of second-generation TSPO tracers to visualize active hand-joint arthritis. Specifically, [^{11}C]DPA-713 and [^{18}F]DPA-714 exhibit lower background uptake than [^{11}C]PK11195, thereby optimizing target-to-background ratios for synovitis detection [63,65,66]. Furthermore, recent RA clinical data indicate that early quantitative [^{11}C]DPA-713 PET/CT measurements, taken at baseline and four weeks after initiating anti-TNF therapy, are associated with clinical disease activity at 26 weeks, highlighting the utility of TSPO-targeted PET as an early therapeutic response biomarker [70]. A key chemical–biological consideration for second-generation scaffolds is their sensitivity to the rs6971 single-nucleotide polymorphism in the human TSPO gene. This genetic variant alters the conformation of the ligand-binding pocket, classifying patients into high-, mixed-, and low-affinity binder groups [67]. Consequently, current radiopharmaceutical research is actively directed toward developing genotype-independent TSPO ligands [63,67–69,71,72]. By strategically modulating aromatic core size, hydrogen-bond acceptor positioning, and steric bulk, modern designs aim to preserve sub-nanomolar affinity while optimizing log $D_{7.4}$, enhancing metabolic stability, and limiting hepatobiliary background [71,73,74].

3.5. Chemokine Receptor CXCR4

CXCR4 is a G protein-coupled receptor. When targeted ligands are used, including high-affinity peptide antagonists, binding occurs through extensive electrostatic interactions deep within a highly negatively charged binding pocket involving residues such as Asp171, Asp262, and Glu288. This interaction induces extremely slow dissociation, corresponding to prolonged receptor residence time. However, the determining factor for the trap model is ligand-induced endocytosis: after ligand binding, the ligand–receptor complex is rapidly internalized through GRK-mediated phosphorylation and β-arrestin recruitment, then translocated to deep endosomes or lysosomes for degradation [75–79].

CXCR4 is a favorable molecular target for PET/CT imaging of synovial inflammation. The most direct support for rheumatoid arthritis (RA) applications comes from the evaluation of [^{18}F]AlF-NOTA-QHA-04 in preclinical arthritis models and human RA synovial tissues, where tracer uptake closely reflects CXCR4-positive inflammatory-cell recruitment and dynamically modulates in response to anti-inflammatory therapy [80]. In parallel, extensive literature on [^{68}Ga]Ga-Pentixafor, [^{64}Cu]Cu-NOTA-pentixather, and therapeutic Pentixather formulations provides a robust foundation regarding CXCR4 radioligand biology, imaging feasibility, and oncology-focused or preclinical theranostic translation [81–86]. Within the context of this review, CXCR4 imaging is emerging as a biomarker for characterizing immune-cell trafficking, disease activity, and treatment response in RA. At the same time, CXCR4-directed radionuclide

therapy remains under evaluation as an investigational concept for benign inflammatory diseases. Compared with conventional imaging modalities, CXCR4-targeted tracers offer a highly specific readout of active immune-cell recruitment when validated within relevant inflammatory models or clinical cohorts [80]. In the management of RA, CXCR4 imaging serves a complementary role alongside other molecular targets: it operates in tandem with FAPI-based assessments of matrix remodeling, TSPO-targeted imaging of macrophage and stromal activation, B-FR imaging of myeloid-lineage inflammation, and integrin $\alpha_v\beta_3$ imaging of synovial angiogenesis. Evidence for ^{177}Lu-Pentixather therapy comes from hematologic malignancies and includes physiologic CXCR4 expression with moderate marrow and splenic exposure; therefore, it needs careful validation regarding the benefit–risk context before therapeutic application in benign RA [85–90].

3.6. Comparative Radiopharmaceutical Profiles

Table 2 shows the chemical characteristics of the designed radioligands, including receptor-targeting motif, radioligand examples, chelator or prosthetic group, binding-affinity class, elimination route, and imaging implications. The citation ranges in this section are used primarily for molecular design and radiochemistry. Direct RA clinical performance is supported only when disease-specific imaging studies are cited; chemistry-only, pharmacokinetic, oncology, or general dosimetry references are treated as background or translational rationale.

Table 2. Comprehensive Molecular Profiles of Synovial-Targeted PET and SPECT Radiopharmaceuticals.

Target Receptor [Ref.]	Radioligand	Bifunctional Chelator/Prosthetic Group & Coordination Core	Binding Affinity (K_d or IC_{50})	Primary Elimination Pathway
FAP [20,26,40,41]	[^{68}Ga]Ga -FAPI-04 FAPI-46 [^{64}Cu]Cu-FAPI-04 [^{99m}Tc]Tc-FAPI-46 [^{99m}Tc]Tc -HYNIC-iFAP	PET: DOTA, NOTA, RESCA, SarAr, TETA SPECT: HYNIC/Tricarbonyl [^{99m}Tc(CO)$_3$]$^+$	Sub-nanomolar (IC_{50}~0.3–0.9 nM)	Renal. FAPI platforms generally provide favorable image contrast; delayed ^{64}Cu imaging remains a chemistry/logistics rationale unless validated in RA.
CXCR4 [81–86]	[^{68}Ga]Ga-Pentixafor [^{18}F]AlF-NOTA-QHA-04	PET: DOTA, NOTA, NODAGA, AlF-NOTA Theranostic: DOTAGA/DOTA analogs	Nanomolar (IC_{50}~5.0–25.0 nM)	Renal. Supports immune-cell and synoviocyte activity mapping; CXCR4-directed therapy in RA remains investigational and requires dedicated dosimetry and safety validation.
Integrin $\alpha_v\beta_3$ [45,49–52]	[^{18}F]Galacto-RGD [^{68}Ga]Ga-RGD2 [^{68}Ga]Ga-PRGD2	PET: DOTA, NOTA, NODAGA, BNOTA, carbohydrate-functionalized or PEGylated linkers	Nanomolar (K_d~1.0–10.0 nM)	Renal/hepatobiliary. RGD cyclization, glycosylation, or PEGylation improves angiogenesis-targeted imaging and periarticular target-to-background ratios.
β-FR [55–60]	[^{68}Ga]Ga-Folate [^{18}F]fluoro-PEG-folate [^{64}Cu]Cu-Folate [^{99m}Tc]Tc-EC20	PET: NOTA, NODAGA, TETA SPECT: Tc(V)-oxo-N_3S core	Nanomolar (K_d~1.0–5.0 nM)	Renal (with high kidney retention). Requires hydrophilic linkers (PEG) to optimize TBR in periarticular tissue.
TSPO [11–13,41,63,65–69,71,72,74]	[^{11}C]PK11195 [^{11}C]PBR28 [^{11}C]DPA-713 [^{18}F]DPA-714 [^{18}F]GE-180 [^{18}F]FEMP	PET: Covalent ^{11}C methylation/carbonylation or ^{18}F substitution	Nanomolar (K_d~2.0–10.0 nM)	Hepatobiliary/Renal. 1st generation suffers from high lipophilicity (log $D_{7.4} > 3$) and high non-specific background. 2nd and 3rd generation improved target-background ratios

4. Translational and Clinical Progress

The clinical translation of target-specific radiopharmaceuticals in rheumatology has rapidly advanced beyond animal validation, establishing a path toward personalized patient management. Elzayat et al. recently highlighted prospective datasets, first-in-human experiences, phase-validation studies, and molecular imaging in RA [72], which reinforce the clinical value of molecular imaging when conventional assessment is discordant with symptoms, serology, or structural imaging. Across RA applications, PET/CT can identify metabolically or target-positive synovitis, quantify multi-joint inflammatory burden, detect extra-articular inflammatory involvement, and monitor treatment response over time. This information supports the transition from single-lesion qualitative interpretation to whole-body or whole-limb quantitative phenotyping, in which tracer selection is guided by the dominant biological process: fibroblast activation, macrophage infiltration, angiogenesis, mitochondrial activation, or chemokine-driven immune-cell recruitment [87].

The clinical translation data compiled in Table 3 underscore progress toward target-specific synovial phenotyping, but the evidence levels differ across targets and tracer classes. For FAP, the most direct RA clinical evidence is provided by [^{99m}Tc]Tc-HYNIC-iFAP (Mexican Health Ministry authorization No. 0564R2025 SSA) (Figure 2) and [^{18}F]FAPI PET/CT studies that enrolled RA patients and evaluated disease activity or treatment response [23]. Other FAP/FAPI studies support ligand hydrophilicity, ligand specificity, fibroinflammatory imaging, or oncology-derived theranostic translation, all of which are relevant to prospective RA clinical performance [20–26,36–38,40,41,88]. Therefore, the transition to FAP-directed radionuclide therapy using ^{177}Lu (e.g., [^{177}Lu]Lu-FAP-2286 [89] and [^{177}Lu]Lu-LNC1004 [90]) remains a potential application until it is directly demonstrated in the RA population.

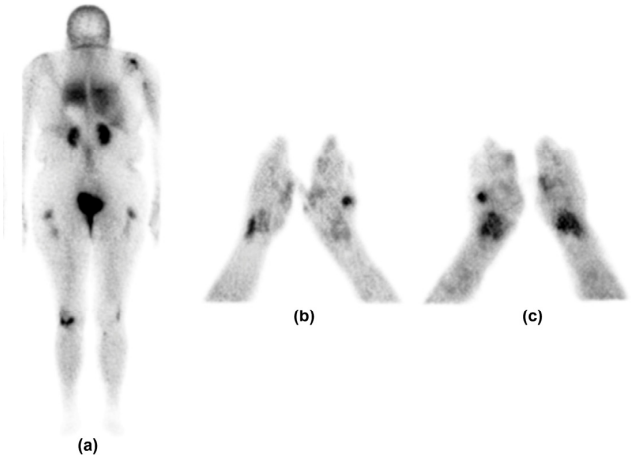


Figure 2. Illustrative (**a**) posterior whole-body SPECT view, and planar images of the hands in (**b**) anterior and (**c**) posterior positions of a patient with rheumatoid arthritis following an intravenous injection of 740 MBq of [^{99m}Tc]Tc-HYNIC-iFAP administered 30 min earlier. Note the uptake of the radiopharmaceutical in the shoulder, hip, knee, wrist and finger joints (Mexican Health Ministry authorization no. 0564R2025 SSA). Written informed consent has been obtained from the patient to publish this paper.

CXCR4 and integrin $\alpha_v\beta_3$ entries extend this interpretation from stromal activation to immune-cell trafficking and angiogenic remodeling. For CXCR4, RA-specific conclusions should rely principally on the study reported by Han et al. [80], which examined CXCR4-targeted PET in arthritis models, human RA synovial tissue, correlations with disease severity, and responses to methotrexate or etanercept. Broader [^{68}Ga]Ga-Pentixafor/[^{177}Lu]Lu-Pentixather radiopharmaceuticals support the CXCR4 radioligand theranostic concept but predominantly outside RA [81–86].

Table 3. Evidence maps for target-specific synovial radiopharmaceuticals, separating direct human RA evidence from translational, preclinical, and chemistry-based evidence.

Target Receptor [Ref.]	Radiopharmaceutical	Clinical Study Design and Cohort	Key Quantitative Metrics and Performance	Translational Significance and Clinical Impact
CXCR4 [80]	[^{18}F]AlF-NOTA-QHA-04	Translational RA study using arthritic mouse models and human RA synovial tissue; therapeutic-response assessment after methotrexate and etanercept treatment.	High CXCR4 specificity; joint uptake correlated with arthritis severity and decreased after treatment-induced remission.	Supports CXCR4 imaging as a disease-activity and treatment-response biomarker for immune-cell–driven synovitis.
Integrin $\alpha_v\beta_3$ [47,48]	[^{68}Ga]Ga-BNOTA-PRGD2/[^{68}Ga]Ga-PRGD2	Open-label RA PET/CT clinical trial and prospective proof-of-concept cohort; 20 untreated active RA patients and 2 osteoarthritis controls, with 12 RA patients rescanned after 3 months of therapy.	Specific synovial uptake in neovascular active inflammation; post-treatment uptake changes correlated with changes in clinical disease activity index.	Establishes $\alpha_v\beta_3$ RGD PET as an angiogenesis-specific clinical imaging tool.
FAP [2,23,36]	[^{68}Ga]Ga-FAPI-04/[^{68}Ga]Ga-FAPI-46/[^{18}F]FAPI PET/CT [^{99m}Tc]Tc-HYNIC-iFAP SPECT/CT	RA-focused clinical and translational evidence supports FAPI PET/CT and HYNIC-iFAP SPECT/CT visualization of active synovitis, disease-activity evaluation, and treatment-response monitoring.	FAP inhibitor uptake localizes fibroblast-rich active synovitis and has been reported to reflect disease activity and treatment response in RA.	Strengthens FAP as a precision-imaging biomarker for activated fibroblast-like synoviocytes in RA.
β-FR [55–60]	[^{99m}Tc]Tc-EC20 (FolateScan)	Single-center, open-label, cross-sectional study: 40 patients with RA, 6 with osteoarthritis, 12 with other inflammatory conditions, and 5 healthy participants.	FolateScan detected more involved joints than clinical swelling or pain/swelling counts in many patients; imaging joint counts correlated with ESR and C-reactive protein. Uptake was also observed in osteoarthritis.	Direct human RA evidence for lesion visualization and association with inflammatory burden.
FAP/Al^{18}F chemistry [16,19,27,28,31,32,46]	[^{18}F]F-AlF-NOTA-FAPI	Chemistry/logistics rationale for fluorine-18 AlF-labeled FAPI derivatives; not yet supported by a direct clinical RA study.	Fluorine-18 can improve PET image sharpness relative to gallium-68 because its positron energy is lower.	Potentially useful for small-joint fibroblast-activation imaging
TSPO [65,66,70]	[^{11}C]DPA-713/[^{18}F]DPA-714/[^{11}C]PK11195	Direct human RA evidence includes proof-of-concept TSPO imaging studies and a separate 20-patient [^{11}C]DPA-713 cohort scanned at baseline and 4 weeks after starting anti-TNF therapy.	In the 20-patient study, joint SUV measures at baseline and week 4 were associated with tender and swollen joint counts at week 26; this supports early response association/prediction, not proven treatment-selection benefit.	For rs6971-sensitive TSPO tracers, genotyping is recommended or protocol-dependent.
FAP/^{64}Cu concept [16,17,29,87]	[^{64}Cu]Cu-NOTA-FAPI [^{64}Cu]Cu-NOTA-iFAP	Proposed diagnostic-to-dosimetry concept based on ^{64}Cu half-life and chelator stability; not yet supported by a direct clinical RA study.	Delayed PET at 12–48 h is chemically plausible for stable ^{64}Cu constructs.	May support residence-time estimation before therapeutic analogs, but conversion to ^{177}Lu or ^{225}Ac therapy remains investigational in RA.

In parallel, integrin $\alpha_v\beta_3$ imaging represents the most mature clinical example of PET targeting angiogenesis in RA. In the prospective proof-of-concept ^{68}Ga-PRGD2 PET/CT cohort, untreated active RA patients showed specific uptake in synovium rich in neovasculature and high $\alpha_v\beta_3$ expression [47,48]. In contrast, uptake changes after treatment correlated more clearly with changes in clinical disease activity than FDG did in settings with muscular uptake [47,48]. The registered ^{68}Ga-BNOTA-PRGD2 clinical trial further reinforces this translational pathway by evaluating the diagnostic performance and treatment response assessment of RGD PET/CT in RA [47,48]. More recent prospective work using angiogenesis-specific ^{68}Ga-RGD2 PET/CT has also compared PET-derived joint metrics with DAS28-ESR, supporting RGD imaging as a quantifiable sensor of vascular remodeling for disease activity and response evaluation [48].

Macrophage-directed clinical translation via [^{99m}Tc]Tc-EC20 shows that SPECT can provide accessible cell-specific information in routine rheumatology; in the FolateScan experience, uptake identified active joints and supported B-FR imaging as a surrogate of activated macrophage burden [55–60]. TSPO PET adds a complementary macrophage/stromal activation axis because RA imaging studies using TSPO tracers have visualized active arthritis of the hand and compared it with other imaging measures [65,66]. Newer [^{11}C]DPA-713 PET/CT data suggest that macrophage-targeted TSPO uptake measured early during anti-TNF therapy may predict later clinical joint activity, supporting TSPO PET as a response-monitoring tool rather than only a diagnostic synovitis marker [70]. TSPO ligand development, neuroinflammation, and rs6971 genotype effects remain scientifically important, although they are not direct evidence from the RA cohort [63,67–69]. Together, FAP, CXCR4, integrin $\alpha_v\beta_3$, B-FR, and TSPO define complementary axes: fibroblast activation, leukocyte trafficking, angiogenesis, macrophage infiltration, and mitochondrial inflammatory activation, which should be selected according to the clinical question and linked to standardized quantitative endpoints for future biologic and targeted synthetic DMARD trials.

The [^{11}C]DPA-713 anti-TNF response study is relevant because it moves TSPO PET from lesion detection toward therapeutic decision support. By evaluating macrophage-targeted uptake at baseline and early during treatment, the study frames TSPO signal as a dynamic biomarker that may anticipate clinical evolution rather than mirror contemporaneous swelling or pain [70]. This study is especially important in RA precision medicine because early separation of likely responders from non-responders could reduce unnecessary biologic exposure and shorten the time to therapeutic adjustment [70].

5. Synovial Theranostics

The management of persistent, localized joint inflammation is undergoing a conceptual shift from passive intra-articular radiocolloids toward molecularly guided synovial theranostics. Conventional radiosynovectomy remains a clinically relevant intervention, delivering β-emitting particulate agents directly into the joint cavity, where the inflamed synovial lining phagocytoses them, inducing local fibrosis, reducing pain, and controlling effusion. However, its mechanism of action is fundamentally a normal physiologic process (e.g., colloid phagocytosis) rather than a molecularly targeted one. Radiocolloids such as ^{90}Y, ^{186}Re, ^{169}Er, or ^{32}P are selected primarily based on joint size, particle retention characteristics, and β-particle range, instead of receptor expression or pathogenic cell phenotypes [21,91–96]. Recent prospective, multicenter evidence confirms that radiosynoviorthesis is both safe and clinically effective for refractory synovitis across various inflammatory arthropathies, including RA.

Targeted RA theranostic radiopharmaceuticals seek to leverage disease-associated molecular structures to link diagnostic phenotyping with targeted radiation delivery or

image-guided interventions. Table 4 summarizes the mechanistic and translational contrast between conventional radiosynovectomy and targeted synovial theranostics. At present, this molecular approach remains investigational in RA, as the current foundation for therapeutic radionuclides is primarily derived from conventional radiosynovectomy, oncological radioligand therapy, dosimetry modeling, and radiochemistry literature rather than completed RA molecular synovial therapy trials [20–29,31–33,36,37,40,41,45,46,49–52,72,88,97]. For instance, Hao et al. describe RA nanoprobes as multifunctional systems that integrate targeting ligands, imaging reporters, anti-inflammatory payloads, and stimulus-responsive components, effectively linking inflammation visualization with guided precision therapy [97]. This concept supports hybrid radiopharmaceutical strategies in which diagnostic signal, target validation, and therapeutic delivery are co-designed. Nevertheless, these advanced platforms are best presented as emerging translational frameworks rather than established clinical nuclear medicine therapies, given that RA-specific radiation dosimetry, biodistribution, long-term articular retention, immunogenicity, and regulatory pathways require further validation and clinical translation.

Table 4. Comparative therapeutic strategies in nuclear medicine: from conventional radiosynovectomy to targeted synovial theranostics.

Feature [Ref.]	Traditional Radiosynovectomy	Targeted Synovial Theranostics
Mechanism [20–29,31–33,36–41,45,46,49–52,89,92–96,98–101]	Intra-articular injection of radioactive colloids or macroaggregates that are retained locally and phagocytosed by synoviocytes or macrophage-rich synovial lining.	Systemic or localized injection of radioligands that actively bind disease-defining targets such as FAP, B-FR, CXCR4, integrin $\alpha_v\beta_3$, or TSPO on pathogenic synovial compartments.
Specificity [20–29,31–33,36–41,45,46,49–52,89,92–94,98–101]	Nonspecific synovial ablation; radiation affects diseased and adjacent synovial lining according to local particle retention and β-particle range.	High molecular specificity; treatment selection can be guided by target expression on activated FLSs, macrophages, immune-cell trafficking pathways, or angiogenic endothelium.
Delivery Route [38–43,91–96]	Strictly local delivery requires direct needle placement into each affected joint.	Potential local or systemic administration, enabling molecular treatment planning for polyarticular disease when organ dosimetry and target retention are acceptable.
Radionuclides [21,89,91–94,96,98–104]	Primarily β-emitting radiocolloids or particulate systems such as ^{90}Y, ^{186}Re, ^{169}Er, ^{32}P, ^{153}Sm-hydroxyapatite / hydroxide macroaggregates, ^{165}Dy, and ^{166}Dy/^{166}Ho in vivo generator systems.	β-emitting and α-emitting molecular radioligands, such as ^{177}Lu- or ^{225}Ac-labeled target-specific synovial ligands, paired with diagnostic PET/SPECT analogs.

Additionally, synovial theranostics faces stricter requirements than oncologic radioligand therapy because rheumatoid arthritis is a chronic, non-malignant disease. Any therapeutic strategy must demonstrate durable joint benefit while delivering minimal absorbed dose to the bone marrow, kidneys, liver, gonads, and whole body, with negligible leakage of the radioligand retained in the synovium. In this context, individualized dosimetry, standardized quantitative imaging, and careful monitoring of organs at risk are essential safety requirements before the use of β- or α-emitting radioligands can be justified in benign inflammatory diseases [21,89,91–94,96,98–104]. Systemic retention outside of the joints is a particular concern, since, for example, low levels of FAP are present in healthy tissues undergoing physiological remodeling, such as in healing wounds and reproductive tis-

sues; this raises the potential for systemic toxicity when FAP-targeted agents move from diagnostic imaging to therapeutic applications [20–26,89,90].

The accumulated experience with radiosynoviorthesis supports a favorable safety profile when established intra-articular protocols are followed; however, a systemic targeted synovial theranostic approach would require specific dosimetric validation [21,89,91–94,96,98–104].

Similarly, the radiochemical transition to ^{177}Lu imposes strict coordination when moving from diagnostic isotopes to β^- therapy. Unlike the smaller radiometals used in diagnostic PET, Lu^{3+} is a larger trivalent lanthanide that requires robust multidentate coordination, usually through DOTA-type macrocycles. In FAP-, CXCR4-, or folate-based vectors, DOTA-based therapeutic design must preserve receptor affinity while preventing the release of free lutetium, because dissociated lanthanides may increase off-synovial exposure in the skeleton, kidneys, or bone marrow [14,89,94,101]. The short-to-intermediate tissue range of ^{177}Lu β-emissions is advantageous for advanced pannus, as it enables cross-fire irradiation across the hyperplastic synovium, extracellular matrix, activated fibroblasts, macrophages, and other infiltrating immune cells, even when receptor expression is heterogeneous [21,89,91–94,96,98–104].

Targeted alpha therapy (TAT) with ^{225}Ac offers a distinct therapeutic rationale, based on very high linear energy transfer over short path lengths of 40 to 100 μm, capable of producing dense ionization and double-strand DNA break within a radius of only a few cell diameters [98–100,103,105]. In early or focal synovitis, this physical profile could, in theory, eliminate pathogenic synovial fibroblasts or macrophage-rich cellular niches while preserving adjacent cartilage and bone. However, ^{225}Ac administration is more complex than ^{177}Lu therapy. As a large trivalent ion, actinium requires chelators capable of forming stable complexes under biologically compatible labeling conditions. Although DOTA remains widely used, it often requires heating and is not always optimal for sensitive biological vectors; therefore, chelators such as MACROPA (N,N′-bis[(6-carboxypyridin-2-yl)methyl]-4,13-diaza-18-crown-6) derivatives have been developed to improve room-temperature complexation, actinium stability, and compatibility with proteins or peptides [98,99,106,107]. The main unresolved safety concern is the redistribution of daughter radionuclides. After α emission, recoil energy may disrupt the bond between the parent radionuclide and the chelator, releasing products such as ^{221}Fr, ^{213}Bi, or ^{209}Pb, which may be redistributed to the kidneys, liver, or bone marrow. In rheumatoid disease, where tolerance for toxicity must be very low, any synovial application of ^{225}Ac would need to demonstrate that the carrier, chelator, formulation, and route of administration retain daughter activity within the joint or intended target tissue [98,99,103,106–111].

Target selection, route of administration, and safety rationale remain decisive in benign disease. The clinical question is not whether therapeutic radionuclides can deliver a cytotoxic dose to the synovial membrane, but whether molecular selection makes that dose biologically justified and spatially safe.

In summary, FAP and CXCR4 seem to be the most favorable β-emitting theranostic targets because they exhibit prolonged tissue retention and have direct diagnostic-therapeutic analogs. B-FR may be useful in diseases with a high macrophage burden, although its utility is limited by physiological folate receptor expression in the kidney and by substantial renal retention. Integrin $\alpha_v\beta_3$ appears better suited for imaging angiogenesis and monitoring treatment response than as an initial therapeutic target, because endothelial expression may overlap with physiological vascular repair. TSPO offers an even narrower therapeutic window, given its broad mitochondrial expression and the genotype-dependent nature of ligand binding, which makes reproducible patient selection more challenging [20–29,31–33,36–41,45,46,49–52,89,92–94,98–101].

6. Mathematical Kinetic Modeling of Synovial Radioligands

To extract quantitative biological parameters, such as receptor density, tracer influx rates, or total distribution volumes, from nuclear imaging of inflamed joints, mathematical kinetic modeling is critical for a potential RA theranostic procedure.

The classification of biomarkers into Class I or Class II biokinetic models in molecular imaging and pharmacokinetic studies, such as PET/SPECT, depends strictly on the ligand dissociation rate (k_{off}) and on the mechanisms of internalization, metabolic trapping, or conformational changes at the molecular level. This section integrates the quantitative modeling framework of the reviewed RA biomarkers (Table 5), delineating compartmental approaches, graphical methods, operational equations, and constraints governing the extraction of the net influx rate (K_i) and total volume of distribution (V_T) for CXCR4, TSPO, FAP, and β-FR radioligands [64,70,88,102,104,108,110,112–118].

For synthesis across targets, target-wide kinetic classification is shown as a mechanistic hypothesis framework rather than as a substitute for tracer-specific model selection. Class I denotes systems expected to show substantial cellular internalization, prolonged receptor residence, or slowly reversible retention (for example selected FAP inhibitors and CXCR4 antagonists); Class II denotes systems dominated by reversible receptor binding and exchange (for example β-FR, and TSPO ligands). This distinction is supported by receptor trafficking and binding biology [34,42–44,54–56,63–67,77–82], but the operational PET model must still be selected for each named compound, tissue, and acquisition window by goodness-of-fit, identifiability, and biological plausibility. Thus, the classification predicts a kinetic tendency; it does not require that every Class I tracer be fitted irreversibly or every Class II tracer identically.

Integrin $\alpha_v\beta_3$ was not included in this section because $\alpha_v\beta_3$ is mainly modeled as a Class II reversible system, since monomeric RGD radiotracers bind and dissociate dynamically, with cellular recycling and without irreversible trapping [44]; however, multivalent designs such as RGD dimers or tetramers can increase avidity, markedly reduce the apparent k_{off}, and induce greater internalization, generating a transitional behavior toward quasi-irreversible Class I models [44,119–121].

Table 5. Molecular differences of synovial biomarkers and their biokinetic classification.

Biomarker [Ref.]	Biokinetic Class	Critical Molecular Factor	Radiotracer Fate
CXCR4 [75–79,122]	Class I: Irreversible	Ligand-induced GPCR endocytosis via arrestins	Lysosomal sequestration and cellular degradation.
FAP [34,35]	Class I: Quasi-irreversible	Extreme-affinity enzymatic inhibition (ultra-slow k_{off})	Prolonged retention in the stromal catalytic pocket.
TSPO [61–64]	Class II: Reversible	Transient mitochondrial binding without endocytosis	Free bidirectional passive diffusion across intra-/extracellular compartments.
β-FR [21,53,54]	Class II: Reversible	Rapid endosomal trafficking and continuous membrane recycling	Dynamic equilibrium through cellular efflux and re-exposure.

6.1. Compartmental Frameworks with Vascular Contributions

Synovial hypervascularity (V_b) increases the volume of blood circulating within the joint region of interest (ROI). To isolate true tissue binding from circulating blood-pool

background, the total PET-measured tissue radioactivity concentration, $C_{\mathrm{PET},}(t)$, is modeled as a vascular-fraction-corrected tissue signal (Equation (1)) [118]:

$$C_{\mathrm{PET}}(t) = (1 - V_b)C_{\mathrm{tissue}}(t) + V_b C_{\mathrm{wb}}(t) \quad (1)$$

where $C_{\mathrm{tissue}}(t)$ represents the combined extravascular tissue compartments $(C_1(t) + C_2(t))$ and $C_{\mathrm{wb}}(t)$ is the total whole-blood radioactivity concentration over time.

The mathematical distinction between these compartmental frameworks is fundamentally driven by the tracer dissociation rate constant, k_4, which governs the escape of the radioligand from the specifically bound tissue compartment (C_2) back into the free tissue compartment (C_1). For Class I tracers, such as FAP- and CXCR4-targeted inhibitors, high-affinity enzymatic engagement or rapid receptor-mediated internalization results in negligible tracer release during the imaging window. This biological trapping suppresses the dissociation pathway, allowing the approximation $k_4 \approx 0$ and justifying an irreversible or quasi-irreversible model. Conversely, Class II tracers, including TSPO and β-FR ligands, undergo dynamic, bidirectional exchange across the cellular membrane. In these systems, a measurable and significant dissociation rate constant $(k_4 > 0)$ ensures that the radioligand maintains a reversible equilibrium with the vascular and interstitial spaces, requiring a fully reversible model configuration to quantify synovial binding accurately.

6.1.1. Class I: Irreversible/Quasi-Irreversible Trap Models (CXCR4 and FAP)

For CXCR4- and FAP-targeted ligands, Patlak-type or quasi-irreversible modeling may be appropriate only when experimental data support tracer retention, scan timing, and biological trapping assumptions. In this review, these models are presented as proposed analytical frameworks for synovial imaging rather than fully validated RA kinetic standards (Equations (2) and (3)) [117]

$$\frac{dC_1(t)}{dt} = K_1 C_p(t) - (k_2 + k_3)C_1(t) \quad (2)$$

where $k_4 \approx 0$:

$$\frac{dC_2(t)}{dt} = k_3 C_1(t) \quad (3)$$

where $C_p(t)$ is the metabolite-corrected arterial plasma input function, K_1 is the plasma-to-tissue influx rate, k_2 is the tissue-to-plasma efflux rate, k_3 represents specific receptor association, and k_4 represents receptor dissociation.

6.1.2. Class II: Reversible Equilibrium Models (TSPO and β-FR)

TSPO ligands and folate-targeted tracers exhibit rapid, fully reversible tissue kinetics with measurable dissociation fractions $(k_4 > 0)$ (Equations (4) and (5)) [66,72,104,105]:

$$\frac{dC_1(t)}{dt} = K_1 C_p(t) - (k_2 + k_3)C_1(t) + k_4 C_2(t) \quad (4)$$

$$\frac{dC_2(t)}{dt} = k_3 C_1(t) - k_4 C_2(t) \quad (5)$$

6.2. Derivation of V_b-Corrected Net Influx Rate (K_i) for CXCR4 and FAP

For tracers exhibiting irreversible trapping on the imaging timescale, the net influx rate macroparameter K_i represents the absolute clearance of the tracer from plasma into the specifically bound/trapped synovial compartment (C_2).

6.2.1. The Operational Equation

Solving the differential equations under steady-state conditions ($t > t^*$) transforms the total PET equation into (Equation (6)):

$$C_{\mathrm{PET}}(t) = (1 - V_b)K_i \int_0^t C_p(\tau)d\tau + (1 - V_b)V_{\mathrm{ND}}C_p(t) + V_b C_{\mathrm{wb}}(t) \quad (6)$$

where the macroparameter is defined as (Equation (7)):

$$K_i = \frac{K_1 k_3}{k_2 + k_3} \quad (7)$$

6.2.2. V_b-Corrected Patlak Linearization

To extract K_i while isolating the joint's local hypervascular contribution, the vascular component is subtracted from the total PET signal prior to dividing by the plasma concentration, $C_p(t)$ (Equation (8)):

To extract K_i while isolating the joint's local hypervascular contribution, the equation is divided by $C_p(t)$ (Equation (8)):

$$\frac{[C_{\mathrm{PET}}(t) - V_b C_{\mathrm{wb}}(t)]}{C_p(t)} = (1 - V_b)K_i \frac{\int_0^t C_p(\tau)d\tau}{C_p(t)} + (1 - V_b)V_{\mathrm{ND}} \quad (8)$$

When plotting $\frac{(C_{\mathrm{PET}}(t) - V_b C_{wb}(t))}{C_p(t)}$ against the stretch time axis $\frac{\int_0^t C_p(\tau)d\tau}{C_p(t)}$, the time-dependent blood contribution is removed. Consequently, the vascular-corrected net influx slope permits direct calculation of K_i (Equation (9)):

$$\mathrm{Slope} = (1 - V_b)K_i$$

$$K_i = \frac{\mathrm{Slope}}{1 - V_b} \quad (9)$$

CXCR4 vs. FAP application should be interpreted qualitatively unless full dynamic data are available. Differences in apparent influx or retention may reflect receptor density, vascular delivery, ligand affinity, internalization, enzymatic engagement, or clearance. They should not be assigned to a single kinetic parameter without tracer-specific validation in RA.

6.3. Derivation of Vb-Corrected Volume of Distribution (V_T) for TSPO and β-FR

For fully reversible ligands, the primary target macroparameter is the total volume of distribution (V_T), which reflects the equilibrium ratio of tracer concentration in tissue relative to metabolite-corrected plasma input and can be estimated using compartmental modeling or Logan graphical analysis after tissue-plasma equilibration [64,70,88,102,104,108,110,112–118].

6.3.1. Definitional Equation (Equation (10))

$$V_T = \frac{K_1}{k_2}\left(1 + \frac{k_3}{k_4}\right) \quad (10)$$

where V_T is calculated directly as the slope of the linear plot.

6.3.2. V_b-Corrected Logan Linearization

To ensure kinetic consistency when applying the Logan graphical method to reversible tracers (e.g., FAP-targeted ligands), the vascular contribution is rigorously accounted for in both the instantaneous and cumulative tissue activity terms. The total PET signal is defined

as $C_{PET}(t) = (1 - V_b)\, C_{tissue}(t) + V_b C_{wb}(t)$. Isolating the true tissue response yields the vascular-corrected linearization (Equation (11)):

$$\frac{\int_0^t [(\tau)d\tau - V_b C_{wb}(\tau)]d\tau}{C_{PET}(t) - V_b C_{wb}(t)} = V_T \left[\frac{(1 - V_b)\int_0^t C_p(\tau)d\tau}{C_{PET}(t) - V_b C_{wb}(t)} \right] + \text{int} \quad (11)$$

TSPO vs. β-FR Application: Folate-targeted tracers (β-FR) possess highly rapid association rates (k_3), but clear through a measurable dissociation parameter (k_4). Logan linearization balances this washout, isolating specific synovial macrophage densities while factoring out the prominent background blood-pool component ($V_b C_{wb}$) seen in early frames.

Table 6 summarizes the principal modeling differences among the selected synovial radioligand classes. It contrasts trapped or quasi-irreversible systems, represented by CXCR4 and FAP-targeted agents, with reversible equilibrium systems, represented by TSPO and β-FR tracers. The comparison highlights which macroparameter is most informative for each target, how vascular fraction and local blood flow can bias PET quantification, and why genotype-dependent TSPO binding requires special consideration during study design.

Table 6. Modeling classes of synovial radioligand kinetics.

Parameter/ Modeling Challenge [64,70,88,102,104,108,110,112–118]	CXCR4 Model	FAP Model	TSPO Model	β-FR Model
Primary Target Metric	K_i (Net influx rate)	K_i (Net trapping influx)	V_T (Total volume of distribution)	V_T (Total volume of distribution)
Kinetic Classification	Irreversible/Trapped	Quasi-Irreversible/Trapped	Fully Reversible	Reversible
Sensitivity to Flow (K_1)	Low-to-moderate. Driven heavily by receptor capture (k_3).	Low. High single-pass extraction rate masks flow variations.	High. Blood flow variations distort baseline SUV (standard uptake value) measurements.	Moderate. Renal clearance pathways affect plasma supply curves.
Vascular Fraction Impact (V_b)	High intercept bias; easily corrected via Patlak line.	Minimal late-phase impact due to rapid tissue clearing.	Extreme. Requires strict vascular scaling due to blood-pool noise.	High background blood signal; requires early-frame fixing.
Genotype Dependency	None. Standard structural expression.	None. Consistent enzymatic binding.	High for rs6971-sensitive tracers; genotyping is recommended or protocol-dependent.	None. Homogeneous receptor architecture.

7. Synovial Therapeutic Dosimetry (^{177}Lu and ^{225}Ac)

To translate the diagnostic kinetic parameters (K_i, V_T, V_b) into therapeutic radiation absorbed doses, the system kinetics are integrated over the unique physical decay constants of Lutetium-177 ($\lambda_{Lu} = 0.00434\ h^{-1}$) and Actinium-225 ($\lambda_{Ac} = 0.00291\ h^{-1}$). This comprehensive model applies the Medical Internal Radiation Dose (MIRD) framework across both therapeutic classes, incorporating a Relative Biological Effectiveness (RBE) factor of 5.0 for all alpha emissions.

The equations below are not presented as patient-specific RA predictions; they define a transparent calculation pathway that can combine measured dynamic imaging, physical decay, biological clearance, tissue mass, and published energy-deposition data. This distinction

permits model-derived comparisons without representing extrapolated values as clinical RA doses. The quantitative translation links the compartmental and graphical modeling framework described above with patient-specific MIRD-based absorbed-dose estimation for candidate synovial theranostic vectors [64,70,88,102,104,108,110,112–118]. The model can apply the MIRD framework across β- and α-emitting therapeutic classes, using biologically weighted estimates for α-particle therapy because high-linear-energy-transfer emissions produce a greater biological effect per unit absorbed dose than β-particle irradiation.

7.1. Generalized MIRD Dosimetry Framework with Kinetic Scaling

The absolute radiation absorbed dose (D_{RBE,r_k}) delivered to a target tissue or organ (r_k) from a self-irradiating radioactive source ($r_k = r_h$) is mathematically structured as (Equation (12)):

$$D_{\mathrm{RBE},r_k} = \mathrm{RBE}_x \cdot \widetilde{A}_{r_k} \cdot S_{\mathrm{self}}(x) \tag{12}$$

where RBEx equals 1.0 for [^{177}Lu]β-particles and 5.0 for [^{225}Ac] α-particles. $S_{\mathrm{self}}(x)$ (self-irradiation S factor) is the mean absorbed dose deposited in the synovium per unit cumulated activity localized within the same tissue. The Time-Integrated Activity ($\tilde{A}_{rk}$) is derived directly by applying Laplace transforms to the dynamic tissue retention curves established by the diagnostic parameters as follows:

7.1.1. For Trapped/Quasi-Irreversible Vectors (CXCR4 and FAP-2286)

Because dissociation from the target tissue is negligible ($k_4 \to 0$), the continuous accumulation component scales directly as a function of the blood-volume corrected net influx rate (K_i) integrated against the decaying plasma concentration curve (Equations (13) and (14)):

$$\widetilde{A}_{\mathrm{tissue}}(x) = A_0 \int_0^{\infty} \left[(1 - V_b) \cdot K_i \int_0^t C_p(\tau) d\tau + (1 - V_b) V_{ND} C_p(t) + V_b C_{wb}(t) \right] e^{-\lambda_x t} dt \tag{13}$$

$$\widetilde{A}_{\mathrm{tissue}}(x) \approx A_0 \cdot (1 - V_b) \cdot \frac{K_i \cdot \mathcal{L}\{C_p(t)\}_{s=\lambda_x}}{\lambda_x} \tag{14}$$

where the time-integrated activity $\widetilde{A}_{tissue}$ has units $MBq \cdot h$; the administered activity A_0 at t = 0 (MBq); C_p denotes the metabolite-corrected plasma activity concentration (MBq·mL^{-1}); V_b is the fractional blood volume within the tissue region of interest (dimensionless); C_{wb} is the time-dependent whole-blood radioactivity concentration (MBq·mL^{-1}); V_{ND} is the nondisplaceable distribution volume and represents freely distributed tracer plus nonspecific binding in tissue (mL·cm^3, equivalent to mL of plasma per mL of tissue); and K_i has units h^{-1}.

$\mathcal{L}$ is the Laplace transform evaluated at the specific radionuclide decay constant $s = \lambda_x$.

7.1.2. For Reversible Dynamic Vectors (TSPO and β-FR)

Because dissociation is active ($k_4 > 0$), the long-term tissue retention tracks a state of dynamic equilibrium governed by the total volume of distribution (V_T) and the overall biological clearance rate of the parent compound from the systemic blood (λ_{bio}) (Equation (15)):

$$\widetilde{A}_{tissue}(x) \approx A_0 \cdot [(1 - V_b) V_T + V_b \cdot \alpha] \cdot \mathcal{L}\{C_p(t)\}_{s=\lambda_x+\lambda_{bio}} \tag{15}$$

where α is defined as the dimensionless tissue-retention or scaling fraction specified for each model; it must not be confused with α-particle radiation. For $S_{\mathrm{self}}(x)$ calculation, the model of the inflamed synovium is considered as a hollow or flattened ellipsoid with a pathological thickness of 1.5–3.5 mm. For ^{177}Lu, a β^- emitter with a tissue range comparable to synovial thickness, a partial absorbed fraction, $\varphi_\beta \approx 0.82$–$0.90$, is applied to account for

local energy escape into the synovial fluid or adjacent cartilage. For ^{225}Ac, an α emitter with a range of 40–90 µm, complete local absorption within the synovium ($\varphi_{\alpha} \equiv 1.0$) is assumed. It is considered a retention of the full progeny contribution for vectors with high cellular internalization, and a reduction in the retention factor for reversible or extracellular tracers to correct for radioactive daughter escape ($f_{ret} \approx 0.30–0.45$) is applied [21,89,93–96,98–102,104,113,115,123,124].

Table 7 compares model-derived, hypothesis-generating absorbed-dose estimates for inflamed synovium and major organs at risk, contrasting β-emitting and α-emitting strategies. The therapeutic index (TI = Dose synovium/Dose critical OAR) suggests that FAP-2286-based vectors may offer the widest operating window because high target retention is paired with comparatively low background tissue exposure. However, this ranking must be interpreted conservatively in benign inflammatory disease and confirmed by patient-specific dosimetry before any activity escalation.

Table 7. Comparative therapeutic dosimetry of candidate synovial theranostic radiopharmaceuticals for β- and α-emitter strategies *.

Radiopharmaceutical [Ref.] (Extrapolated Considerations)	Inflamed Synovium (Target Tissue)	Kidneys (OAR)	Liver (OAR)	Spleen (OAR)	Red Bone Marrow (OAR)
[^{177}Lu]Lu-Pentixather [3,4,80–86,94,108,110,125] (CXCR4; model-derived Gy/GBq)	3.50–12.50	0.45–0.91	0.63–0.71	0.58	0.47
[^{225}Ac]Ac-Pentixafor [14,80–86,98–100,105–107,109]. (CXCR4; theoretical/model-derived Gy_{RBE}/MBq). Calculations require experimental microdosimetry	0.220–0.650	0.075	0.012	0.038	0.008
[^{177}Lu]Lu-FAP-2286 [89,94,101,108,110,112,124] (FAP; oncology-informed/model-derived Gy/GBq)	4.10–14.80	1.00	0.12	0.06	0.05
[^{225}Ac]Ac-FAP-2286 [14,98–100,106–110] (FAP; theoretical/model-derived Gy_{RBE}/MBq)	0.310–0.820	0.115	0.009	0.004	0.002
TSPO therapeutic construct [63,65–67,69,72,102,104,108,110,115] (conceptual/model-derived Gy/GBq)	0.85–2.10	0.45	1.55	0.30	0.12
TSPO alpha-emitter concept [63,65–69,71,72,74,98–100,103,105] (theoretical/model-derived Gy_{RBE}/MBq)	0.045–0.095	0.088	0.110	0.015	0.004
Folate therapeutic concept [55–58,60,94,101,108,110] (β-FR; model-derived Gy/GBq)	1.20–3.80	3.50	0.22	0.08	0.15
Folate alpha-emitter concept [14,55–60,98–100,103,105–110] (β-FR; theoretical/model-derived Gy_{RBE}/MBq)	0.075–0.180	0.420	0.018	0.006	0.011

* Values are model-derived estimates. They integrate diagnostic uptake assumptions, oncology radioligand-therapy experience, radiosynovectomy safety logic, and MIRD-based scaling; they require RA-specific residence-time measurements, organ-at-risk dosimetry, and safety validation before clinical translation [64,70,88,102,104,108,110,112–118].

Although this review generally focuses on radiotracers for PET and SPECT, it is worth mentioning the development of radiolabeled nanoparticles for molecular imaging. Matrix

metalloproteinases (MMPs) (particularly MMP-1, MMP-2, MMP-3, MMP-9, and MMP-13) are overexpressed in joint tissue and inflamed synovium in RA and osteoarthritis, where they degrade collagen, aggrecan, and the extracellular matrix. Therefore, some systems based on nanoparticles decorated with specific-recognition peptides labeled with ^{64}Cu have recently been reported as efficient radio-systems for molecular imaging [126,127].

8. Conclusions and Future Perspectives

The development of target-specific PET and SPECT radiopharmaceuticals has transformed rheumatoid arthritis research, particularly in imaging. This progress has advanced the field from a stage of descriptive inflammation assessment to a new era of mechanism-based precision medicine. The evidence presented here demonstrates that radiochemistry, molecular target selection, clinical imaging, kinetic modeling, and dosimetry have already converged into a coherent framework for identifying the cellular drivers of active synovial disease before irreversible structural damage becomes dominant. A critical accomplishment in this field is the ability to compartmentalize synovitis into a series of imageable molecular subdivisions. FAP identifies activated fibroblast-like synoviocytes and matrix remodeling; β-FR reveals the presence of macrophages and the extent of their inflammatory burden; TSPO reports mitochondrial activation in stromal and myeloid cells; CXCR4 monitors the recruitment of immune cells driven by chemokines; and integrin $\boldsymbol{\alpha_v\beta_3}$ captures angiogenic pannus expansion.

A significant advance has been the evolution of radiopharmaceutical chemistry into a practical design discipline for rheumatology, based on prior oncology experience. It is evident that the selection of chelators, the architecture of linkers, the half-life of radionuclides, the stability of coordination, hydrophilicity, and clearance routes are determining factors in biological performance, rather than being secondary technical details. This knowledge has enabled the development of PET and SPECT radiopharmaceuticals based on ^{68}Ga, ^{18}F/[Al^{18}F]$^{2+}$, ^{64}Cu, ^{99m}Tc, and ^{11}C that can be matched rationally to FAP, CXCR4, B-FR, TSPO, and integrin-targeted ligands. Consequently, the field has acquired a versatile chemical toolbox that supports both high-resolution PET phenotyping and accessible SPECT/CT implementation.

The translation of these radiopharmaceuticals has also resulted in operational benefits. Fluorine-18 AlF strategies have expanded the scalability of FAPI probes for RA imaging. At the same time, [^{99m}Tc]Tc-HYNIC and folate-based agents have demonstrated that target-specific molecular imaging for synovitis can be adapted to widely available SPECT infrastructure. Concurrently, ^{64}Cu constructs enable longer imaging windows for estimating residence time. Furthermore, the use of ^{11}C or ^{18}F TSPO tracers has notably enhanced imaging of macrophage and stromal activation. Collectively, these advances support a realistic clinical scenario in which PET and SPECT are not competing approaches but complementary technologies selected according to target biology, joint size, logistical access, and the clinical question under investigation.

The review of relevant studies demonstrated that molecular imaging is beginning to deliver actionable biological phenotyping in rheumatoid arthritis. FAPI PET and SPECT have demonstrated the capacity to visualize fibroblast-rich active synovitis and monitor disease activity or treatment response. CXCR4-targeted imaging has linked immune-cell trafficking with disease severity and therapeutic modulation. RGD-based integrin PET has provided a functional measure of synovial angiogenesis. Folate-targeted SPECT and PET have validated macrophage-directed imaging. TSPO PET has advanced from lesion visualization toward early response assessment during biologic therapy. The aforementioned achievements establish molecular imaging as a mechanistic layer that complements MRI, musculoskeletal

ultrasound, serology, and clinical scores by revealing pathogenic processes that conventional tools cannot resolve directly.

A particularly pertinent perspective concerns the emerging use of target selection as a decision-support strategy. Instead of anticipating a single radiotracer to encompass the comprehensive array of dimensions inherent to RA, the extant evidence supports a targeted, question-driven approach. FAPI tracers have been demonstrated to be most effective in the context of fibroblast-driven pannus remodeling; CXCR4 probes are effective in terms of immune-cell recruitment and treatment-response monitoring; B-FR and TSPO tracers have been demonstrated to be effective in terms of macrophage or mitochondrial inflammatory activation; and RGD-based ligands are effective in terms of angiogenic remodeling. This logic establishes a basis for future synovial theranostic interventions, enabling patient selection based on the predominant molecular pathotype rather than solely on clinical activity scores.

The field's quantitative dimension has also advanced substantially. Static SUV-based measurements already provide clinically useful information, while dynamic acquisitions, vascular-fraction correction, Patlak-type analysis, Logan modeling, and MIRD-based dosimetric translation create a pathway from diagnostic imaging to individualized therapeutic planning. In this review, the integration of these methods was undertaken to demonstrate the interpretation of quasi-trapped FAP and CXCR4 vectors, reversible TSPO and B-FR tracers, and angiogenesis-targeted integrin probes within target-specific kinetic frameworks. This quantitative foundation is essential for converting molecular images into reproducible biomarkers, response endpoints, residence-time estimates, and eventually patient-specific synovial dose planning.

The theranostic perspective represents a significant conceptual advancement. Conventional radiosynoviorthesis has already demonstrated the clinical value of local nuclear medicine approaches for refractory synovitis, and the emergence of target-specific radioligands now extends this principle toward molecularly guided synovial micro-radioresection. The utilization of β-emitting vectors based on ^{177}Lu, in conjunction with α-emitting strategies based on ^{225}Ac, offers a robust therapeutic framework when complemented by diagnostic confirmation of target expression, residence-time evaluation, and organ-at-risk dosimetry. Advancements in chelators, including DOTA-type scaffolds, cross-bridged polyamines, and MACROPA, reinforce the chemical underpinnings of stable therapeutic radiometal delivery. This progression signifies a future in which treatment intensity can be guided by the same molecular probes used for diagnostics.

The incorporation of reviews and clinical studies further substantiates this optimistic translational trajectory. The ^{99m}Tc literature highlights accessibility and the implementation of kit-based SPECT/CT. Recent PET/CT reviews emphasize whole-body assessment of disease activity and treatment monitoring. The [^{11}C]DPA-713 anti-TNF study strengthens the role of early macrophage-targeted response biomarkers. Theranostic nanoprobes expand the horizon towards integrated visualization and image-guided intervention. Collectively, these developments demonstrate that molecular imaging in RA is evolving beyond its traditional role as a mere exploratory visualization tool. Instead, it is progressing towards a comprehensive framework that integrates diagnosis, phenotyping, response prediction and therapy planning.

The subsequent phase should build on these accomplishments by implementing harmonized multicenter protocols, standardized injection activities and uptake times, consistent joint-segmentation methods, validated target-to-background and kinetic endpoints, and clinically meaningful outcome measures. It is asserted that these steps will not merely address technical variability; they will enable comparison across sites, strengthen regulatory acceptance, and accelerate incorporation of target-specific radiopharmaceuticals into preci-

sion rheumatology trials. In this implementation pathway, molecular imaging should serve as a biological decision layer that complements structural imaging and clinical assessment, enabling earlier recognition of residual pannus activity, more rational treatment escalation or de-escalation, and more efficient evaluation of new targeted therapies.

In conclusion, this review demonstrated that synovial-targeted radiopharmaceuticals have attained a level of chemical, biological, and translational maturity that has the potential to significantly impact the evaluation of RA and related inflammatory arthropathies. The field has already achieved several major achievements, including the target-specific visualization of fibroblast activation, macrophage burden, mitochondrial inflammatory activation, immune cell trafficking, and angiogenesis. Furthermore, practical PET and SPECT radiopharmaceuticals have been developed, and there is evidence of clinical disease activity and of monitoring treatment response. Finally, a quantitative framework for kinetic interpretation and dosimetric translation has been established. These accomplishments establish a robust foundation for the next generation of precision rheumatology, in which molecular imaging enables mechanism-based patient selection, early therapeutic-response prediction, and meticulously controlled synovial theranostic strategies. Instead of representing an unmet promise, targeted radiopharmaceuticals now constitute an advancing bench-to-bedside platform capable of transforming inflammatory joint disease from a clinically scored syndrome into a molecularly defined, image-guided, and individually managed condition.

Author Contributions: Conceptualization, G.F.-F.; methodology, M.L.-G., B.O.-G., E.A.-V., L.M.-A. and G.F.-F.; formal analysis, M.L.-G., B.O.-G., E.A.-V., L.M.-A. and G.F.-F.; writing—original draft preparation, M.L.-G., L.M.-A. and G.F.-F.; writing—review and editing, G.F.-F. All authors are responsible for all aspects of the work. All authors have read and agreed to the published version of the manuscript.

Funding: This research was funded by the "Consejo Mexiquense de Ciencia y Tecnología" (COMECyT) through the EDOMEX financing program for female scientists, grant number CIKAS-FICDTEM-25-026 and received Ricerca Corrente funding from the Italian Ministry of Health to cover publication costs.

Institutional Review Board Statement: The study was conducted in accordance with the Declaration of Helsinki and approved for human use by the Mexican Health Regulatory Authority: "Federal Commission for the Protection against Sanitary Risks (COFEPRIS)" (Health registration No. 0564R2025 SSA).

Informed Consent Statement: Written informed consent has been obtained from the patient to publish this paper.

Data Availability Statement: No new data were created or analyzed in this study. Data sharing is not applicable to this article.

Acknowledgments: The authors would like to express their gratitude to Rodrigo Hernández-Ramírez from the Department of Nuclear Medicine at the National Institute of Medical Science and Nutrition Salvador Zubirán for providing, as a courtesy, the clinical image in Figure 2. ^{99m}Tc-HYNIC-iFAP is approved for human use by the Mexican regulatory authority (COFEPRIS) under health registration no. 0564R2025 SSA. Written informed consent has been obtained from the patient to publish this paper. Figure 1 was created specifically for the present manuscript and was not copied, reproduced, or adapted from any previously published work. ChatGPT mod. GTP-6 plus was used to assist with the color palette, and the figure was created under BioRender license agreement No. JH2A2D492M. During preparation of this manuscript, Grammarly and Microsoft Copilot (Office 365) were used to support language editing, writing revision, and conversion of selected LaTeX-formatted equations into Word format. The authors reviewed and edited the content as needed and take full responsibility for the final version of the manuscript.

Conflicts of Interest: The authors declare no conflicts of interest.

Abbreviations

The following abbreviations are used in this manuscript:

ACPA	Anti-citrullinated protein antibody
Al18F	Aluminum fluoride-18 labeling system
BNOTA	Bifunctional NOTA-based chelator
CB-TE2A	4,11-Bis(carboxymethyl)-1,4,8,11-tetraazabicyclo[6.6.2]hexadecane
CXCR4	C-X-C chemokine receptor type 4
DAS28	Disease Activity Score in 28 joints
DCE-MRI	Dynamic contrast-enhanced magnetic resonance imaging
DMARD	Disease-modifying antirheumatic drug
DOTA	1,4,7,10-Tetraazacyclododecane-1,4,7,10-tetraacetic acid
EDDA	Ethylenediamine-N,N′-diacetic acid
EANM	European Association of Nuclear Medicine
FAP	Fibroblast activation protein
FAPI	Fibroblast activation protein inhibitor
FDG	Fluorodeoxyglucose
FLV	FAPI lesion volume
FLS	Fibroblast-like synoviocyte
β-FR	Folate receptor beta
Gy	Gray
HYNIC	6-Hydrazinonicotinamide
IC50	Half-maximal inhibitory concentration
LET	Linear energy transfer
MAG3	Mercaptoacetyltriglycine
MACROPA	N,N′-bis[(6-carboxypyridin-2-yl)methyl]-4,13-diaza-18-crown-6
MIRD	Medical Internal Radiation Dose
MRI	Magnetic resonance imaging
MSUS	Musculoskeletal ultrasound
NODAGA	1,4,7-Triazacyclononane-1-glutaric acid-4,7-acetic acid
NOTA	1,4,7-Triazacyclononane-1,4,7-triacetic acid
OAR	Organ at risk
PET	Positron emission tomography
RA	Rheumatoid arthritis
RESCA	Restrained complexing agent
RGD	Arginine-glycine-aspartate
ROI	Region of interest
SarAr	Sarcophagine chelator
SDAI	Simplified Disease Activity Index
SPECT	Single-photon emission computed tomography
SUV	Standardized uptake value
TAT	Targeted alpha therapy
TBR	Target-to-background ratio
TETA	1,4,8,11-Tetraazacyclotetradecane-1,4,8,11-tetraacetic acid
TI	Therapeutic index
TLF	Total lesion FAPI uptake
TNF	Tumor necrosis factor
TSPO	18 kDa translocator protein
VT	Total volume of distribution

References

1. Black, R.J.; Cross, M.; Haile, L.M.; Culbreth, G.T.; Steinmetz, J.D.; Hagins, H.; Kopec, J.A.; Brooks, P.M.; Woolf, A.D.; Ong, K.L. Global, regional, and national burden of rheumatoid arthritis, 1990–2020, and projections to 2050: A systematic analysis of the Global Burden of Disease Study 2021. *Lancet Rheumatol*. **2023**, *5*, e594–e610. [CrossRef] [PubMed]
2. Colebatch, A.N.; Edwards, C.J.; Østergaard, M.; van der Heijde, D.; Balint, P.V.; D'Agostino, M.A.; Forslind, K.; Grassi, W.; Haavardsholm, E.A.; Haugeberg, G.; et al. EULAR recommendations for the use of imaging of the joints in the clinical management of rheumatoid arthritis. *Ann. Rheum. Dis.* **2013**, *72*, 804–814. [CrossRef] [PubMed]

3. Smolen, J.S.; Edwards, C.J.; Konzett, V.; Laskou, F.; Aletaha, D.; Caporali, R.; Dörner, T.; Hyrich, K.L.; Mateus, E.; Pope, J.E.; et al. EULAR recommendations for the management of rheumatoid arthritis with synthetic and biologic disease-modifying antirheumatic drugs: 2025 update. *Ann. Rheum. Dis.* **2026**, *85*, 991–1009. [CrossRef] [PubMed]
4. Firestein, G.S.; McInnes, I.B. Immunopathogenesis of Rheumatoid Arthritis. *Immunity* **2017**, *46*, 183–196. [CrossRef] [PubMed]
5. Pitzalis, C.; Choy, E.H.S.; Buch, M.H. Transforming clinical trials in rheumatology: Towards patient-centric precision medicine. *Nat. Rev. Rheumatol.* **2020**, *16*, 590–599. [CrossRef] [PubMed]
6. Humby, F.; Lewis, M.; Ramamoorthi, N.; Hackney, J.A.; Barnes, M.R.; Bombardieri, M.; Setiadi, A.F.; Kelly, S.; Bene, F.; DiCicco, M.; et al. Synovial cellular and molecular signatures stratify clinical response to csDMARD therapy and predict radiographic progression in early rheumatoid arthritis patients. *Ann. Rheum. Dis.* **2019**, *78*, 761–772. [CrossRef] [PubMed]
7. Humby, F.; Mahto, A.; Ahmed, M.; Barr, A.; Kelly, S.; Buch, M.; Pitzalis, C.; Conaghan, P.G. The Relationship Between Synovial Pathobiology and Magnetic Resonance Imaging Abnormalities in Rheumatoid Arthritis: A Systematic Review. *J. Rheumatol.* **2017**, *44*, 1311–1324. [CrossRef] [PubMed]
8. Asadoorian, M.; Matcuk, G.R., Jr.; Patel, D.B.; Tomasian, A.; Wassef, H.R.; White, E.A. Musculoskeletal Pitfalls on Fluorodeoxyglucose F 18 PET-Computed Tomography: Pictorial Review. *PET Clin.* **2018**, *13*, 587–607. [CrossRef] [PubMed]
9. Bartok, B.; Firestein, G.S. Fibroblast-like synoviocytes: Key effector cells in rheumatoid arthritis. *Immunol. Rev.* **2010**, *233*, 233–255. [CrossRef] [PubMed]
10. Udalova, I.A.; Mantovani, A.; Feldmann, M. Macrophage heterogeneity in the context of rheumatoid arthritis. *Nat. Rev. Rheumatol.* **2016**, *12*, 472–485. [CrossRef] [PubMed]
11. Pees, A.; Chassé, M.; Lindberg, A.; Vasdev, N. Recent Developments in Carbon-11 Chemistry and Applications for First-In-Human PET Studies. *Molecules* **2023**, *28*, 931. [CrossRef] [PubMed]
12. Fujita, M.; Kobayashi, M.; Ikawa, M.; Gunn, R.N.; Rabiner, E.A.; Owen, D.R.; Zoghbi, S.S.; Haskali, M.B.; Telu, S.; Pike, V.W.; et al. Comparison of four (11)C-labeled PET ligands to quantify translocator protein 18 kDa (TSPO) in human brain: (R)-PK11195, PBR28, DPA-713, and ER176-based on recent publications that measured specific-to-non-displaceable ratios. *EJNMMI Res.* **2017**, *7*, 84. [CrossRef] [PubMed]
13. Doorduin, J.; Klein, H.C.; Dierckx, R.A.; James, M.; Kassiou, M.; de Vries, E.F. [11C]-DPA-713 and [18F]-DPA-714 as new PET tracers for TSPO: A comparison with [11C]-(R)-PK11195 in a rat model of herpes encephalitis. *Mol. Imaging Biol.* **2009**, *11*, 386–398. [CrossRef] [PubMed]
14. Wadas, T.J.; Wong, E.H.; Weisman, G.R.; Anderson, C.J. Coordinating radiometals of copper, gallium, indium, yttrium, and zirconium for PET and SPECT imaging of disease. *Chem. Rev.* **2010**, *110*, 2858–2902. [CrossRef] [PubMed]
15. Davey, P.; Paterson, B.M. Modern Developments in Bifunctional Chelator Design for Gallium Radiopharmaceuticals. *Molecules* **2022**, *28*, 203. [CrossRef] [PubMed]
16. Zhang, X.; Lee, K.C.; Choi, J.Y.; Lee, K.H.; Choe, Y.S. Comparative Study of Dimeric Fibroblast Activation Protein-Targeting Radioligands Labeled with Fluorine-18, Copper-64, and Gallium-68. *Mol. Pharm.* **2025**, *22*, 906–917. [CrossRef] [PubMed]
17. Liu, S.; Li, Z.; Conti, P.S. Development of multi-functional chelators based on sarcophagine cages. *Molecules* **2014**, *19*, 4246–4255. [CrossRef] [PubMed]
18. Boschi, A.; Uccelli, L.; Martini, P. A picture of modern Tc-99m radiopharmaceuticals: Production, chemistry, and applications in molecular imaging. *Appl. Sci.* **2019**, *9*, 2526. [CrossRef]
19. Archibald, S.J.; Allott, L. The aluminium-[18F] fluoride revolution: Simple radiochemistry with a big impact for radiolabelled biomolecules. *EJNMMI Radiopharm. Chem.* **2021**, *6*, 30. [CrossRef] [PubMed]
20. Narain, R.; Nessler, I.; Richardson, P.L.; Erickson, J.E.; Wang, Y.; Ferri, J.; Knight, H.L.; Bryant, S.H.; Phillips, L.A.; Zhang, L.; et al. Increased imaging ligand hydrophilicity and improved pharmacokinetic properties provides enhanced in vivo targeting of fibroblast activation protein. *npj Imaging* **2024**, *2*, 24. Erratum in *npj Imaging* **2025**, *3*, 10. https://doi.org/10.1038/s44303-025-00072-4. [CrossRef] [PubMed]
21. Desaulniers, M.; Rousseau, É.; Pabst, K.M. Clinical and research applications of fibroblast activation protein-α inhibitor tracers: A review. *Br. J. Radiol.* **2026**, *99*, 1263–1270. [CrossRef] [PubMed]
22. Zhang, N.; Pan, F.; Pan, L.; Diao, W.; Su, F.; Huang, R.; Yang, B.; Li, Y.; Qi, Z.; Zhang, W.; et al. Synthesis, radiolabeling, and evaluation of a (4-quinolinoyl)glycyl-2-cyanopyrrolidine analogue for fibroblast activation protein (FAP) PET imaging. *Front. Bioeng. Biotechnol.* **2023**, *11*, 1167329. [CrossRef] [PubMed]
23. Mu, X.; Zhang, F.; Li, M.; Lu, L.; Mo, B.; Li, B.; Yang, M.; Fu, W. Fibroblast activation imaging in rheumatoid arthritis: Evaluating disease activity and treatment response using [18F] FAPI PET/CT. *Eur. Radiol.* **2025**, *35*, 6104–6114. [CrossRef] [PubMed]
24. Trujillo-Benítez, D.; Luna-Gutiérrez, M.; Ferro-Flores, G.; Ocampo-García, B.; Santos-Cuevas, C.; Bravo-Villegas, G.; Morales-Ávila, E.; Cruz-Nova, P.; Díaz-Nieto, L.; García-Quiroz, J.; et al. Design, Synthesis and Preclinical Assessment of (99m)Tc-iFAP for In Vivo Fibroblast Activation Protein (FAP) Imaging. *Molecules* **2022**, *27*, 264. [CrossRef] [PubMed]
25. Ma, M.; Yang, G.; Zhao, M.; Liu, Y.; Ge, X.; Jia, B.; Gao, S. Synthesis and Preliminary Study of (99m)Tc-Labeled HYNIC-FAPi for Imaging of Fibroblast Activation Proteins in Tumors. *Mol. Pharm.* **2024**, *21*, 735–744. [CrossRef] [PubMed]

26. Jiang, Y.; Tian, Y.; Feng, B.; Zhao, T.; Du, L.; Yu, X.; Zhao, Q. A novel molecular imaging probe [99mTc] Tc-HYNIC-FAPI targeting cancer-associated fibroblasts. *Sci. Rep.* **2023**, *13*, 3700. [CrossRef] [PubMed]
27. Rong, J.; Haider, A.; Jeppesen, T.E.; Josephson, L.; Liang, S.H. Radiochemistry for positron emission tomography. *Nat. Commun.* **2023**, *14*, 3257. [CrossRef] [PubMed]
28. Chambers, C.G.; Wang, J.; Sakr, T.M.; Miao, Y.; Smith, C.J. NOTA and NODAGA Radionuclide Complexing Agents: Versatile Approaches for Advancements in Radiochemistry. *Molecules* **2025**, *30*, 2095. [CrossRef] [PubMed]
29. Krasnovskaya, O.O.; Abramchuck, D.; Erofeev, A.; Gorelkin, P.; Kuznetsov, A.; Shemukhin, A.; Beloglazkina, E.K. Recent Advances in (64)Cu/(67)Cu-Based Radiopharmaceuticals. *Int. J. Mol. Sci.* **2023**, *24*, 9154. [CrossRef] [PubMed]
30. Ali, M.; Benfante, V.; Di Raimondo, D.; Laudicella, R.; Tuttolomondo, A.; Comelli, A. A Review of Advances in Molecular Imaging of Rheumatoid Arthritis: From In Vitro to Clinic Applications Using Radiolabeled Targeting Vectors with Technetium-99m. *Life* **2024**, *14*, 751. [CrossRef] [PubMed]
31. Gao, H.; Ma, Z.; Zhu, Z.; Yang, Z.; Chen, B.; Wu, X.; Jakobsson, V.; Deng, Y.; Wang, H.; Zhang, W. Comparative study of [18F] AlF-NOTA-FAPI-RGD and [18F] FDG/[18F] AlF-NOTA-FAPI-04 PET/CT in renal cell carcinoma. *Theranostics* **2025**, *15*, 5790. [PubMed]
32. Bailly, M.; Dupont, A.C.; Domain, G.; Darsin-Bettinger, D.; Courtehoux, M.; Metrard, G.; Manrique, A.; Vigne, J. Gallium-labeled PET radiopharmaceuticals in cardiovascular disease. *Pharmaceuticals* **2025**, *18*, 387. [CrossRef] [PubMed]
33. Tanwar, K.S.; Pandey, M.K. Gallium-68-labeled radiopharmaceuticals: A review. *Chem. Soc. Rev.* **2025**, *54*, 7421–7483. [CrossRef] [PubMed]
34. Loktev, A.; Lindner, T.; Burger, E.-M.; Altmann, A.; Giesel, F.; Kratochwil, C.; Debus, J.; Marmé, F.; Jäger, D.; Mier, W.; et al. Development of Fibroblast Activation Protein–Targeted Radiotracers with Improved Tumor Retention. *J. Nucl. Med.* **2019**, *60*, 1421. [CrossRef] [PubMed]
35. Riaza Montes, M.; Suárez, B.; Solano-Iturri, J.D.; Lecumberri, D.; Iturregui, A.M.; Lawrie, C.H.; Armesto, M.; Nunes-Xavier, C.E.; Pulido, R.; López, J.I.; et al. Fibroblast Activation Protein Alpha (FAP) Expression Is Associated with Disease Recurrence and Poor Response to Tyrosine Kinase Inhibitors in Advanced Clear Cell Renal Cell Carcinoma. *Int. J. Mol. Sci.* **2025**, *26*, 11112. [CrossRef] [PubMed]
36. Huang, Y.; Wu, Y.; Liu, H.; Chen, Y.; Xie, Q.; Yin, G. Targeting fibroblast activation protein in rheumatoid arthritis: From molecular imaging to precision therapeutics. *Front. Immunol.* **2025**, *16*, 1616618. [CrossRef] [PubMed]
37. Panagiotidis, E.; Koinis, F.; Zhang-Yin, J.; Angelidis, G.; Valotassiou, V.; Tsougos, I.; Kotsakis, A.; Georgoulias, P. Fibroblast Activation Protein Inhibitor (FAPI) PET: A Scoping Review of Emerging Oncologic and Fibroinflammatory Applications. *Diagnostics* **2026**, *16*, 1542. [CrossRef] [PubMed]
38. Luo, Y.; Pan, Q.; Zhang, W.; Li, F. Intense FAPI uptake in inflammation may mask the tumor activity of pancreatic cancer in 68Ga-FAPI PET/CT. *Clin. Nucl. Med.* **2020**, *45*, 310–311. [CrossRef] [PubMed]
39. Jafari, E.; Zarei, A.; Dadgar, H.; Keshavarz, A.; Manafi-Farid, R.; Rostami, H.; Assadi, M. A convolutional neural network–based system for fully automatic segmentation of whole-body [68Ga] Ga-PSMA PET images in prostate cancer. *Eur. J. Nucl. Med. Mol. Imaging* **2024**, *51*, 1476–1487. [CrossRef] [PubMed]
40. Albano, D.; Rizzo, A.; Slart, R.H.; Hess, S.; Noriega-Álvarez, E.; Wakfie-Corieh, C.G.; Leccisotti, L.; Glaudemans, A.W.; Gheysens, O.; Treglia, G. The role of fibroblast activation protein inhibitor positron emission tomography in inflammatory and infectious diseases: An updated systematic review. *Pharmaceuticals* **2024**, *17*, 716. [CrossRef] [PubMed]
41. Lindner, T.; Altmann, A.; Giesel, F.; Kratochwil, C.; Kleist, C.; Krämer, S.; Mier, W.; Cardinale, J.; Kauczor, H.-U.; Jäger, D. 18F-labeled tracers targeting fibroblast activation protein. *EJNMMI Radiopharm. Chem.* **2021**, *6*, 26. [CrossRef] [PubMed]
42. Lucie, S.; Elisabeth, G.; Stéphanie, F.; Guy, S.; Amandine, H.; Corinne, A.-R.; Didier, B.; Catherine, S.; Alexeï, G.; Pascal, D.; et al. Clustering and Internalization of Integrin αvβ3 With a Tetrameric RGD-synthetic Peptide. *Mol. Ther.* **2009**, *17*, 837–843. Corrigendum in *Mol. Ther.* **2009**, *17*, 1301. https://doi.org/10.1038/mt.2009.109. [CrossRef] [PubMed]
43. Mittra, E.S.; Goris, M.L.; Iagaru, A.H.; Kardan, A.; Burton, L.; Berganos, R.; Chang, E.; Liu, S.; Shen, B.; Chin, F.T.; et al. Pilot pharmacokinetic and dosimetric studies of (18)F-FPPRGD2: A PET radiopharmaceutical agent for imaging α(v)β(3) integrin levels. *Radiology* **2011**, *260*, 182–191. [CrossRef] [PubMed]
44. Guo, N.; Lang, L.; Gao, H.; Niu, G.; Kiesewetter, D.O.; Xie, Q.; Chen, X. Quantitative analysis and parametric imaging of 18F-labeled monomeric and dimeric RGD peptides using compartment model. *Mol. Imaging Biol.* **2012**, *14*, 743–752. [CrossRef] [PubMed]
45. Notni, J.; Gassert, F.T.; Steiger, K.; Sommer, P.; Weichert, W.; Rummeny, E.J.; Schwaiger, M.; Kessler, H.; Meier, R.; Kimm, M.A. In vivo imaging of early stages of rheumatoid arthritis by α5β1-integrin-targeted positron emission tomography. *EJNMMI Res.* **2019**, *9*, 87. Erratum in *EJNMMI Res.* **2019**, *9*, 107. https://doi.org/10.1186/s13550-019-0582-x. [CrossRef] [PubMed]
46. Wang, H.; Sun, Y.; Wu, C.; Zhu, Z. ^{68}Ga-BNOTA-PRGD2 PET/CT for evaluation of post-stroke angiogenesis: Study protocol for a prospective open-label clinical trial. *Asia Pac. J. Clin. Trials Nerv. Syst. Dis.* **2016**, *1*, 43. [CrossRef]

47. Zhu, Z.; Yin, Y.; Zheng, K.; Li, F.; Chen, X.; Zhang, F.; Zhang, X. Evaluation of synovial angiogenesis in patients with rheumatoid arthritis using 68Ga-PRGD2 PET/CT: A prospective proof-of-concept cohort study. *Ann. Rheum. Dis.* **2014**, *73*, 1269–1272. [CrossRef] [PubMed]
48. Kavanal, A.J.; Bhattacharya, A.; Sharma, A.; Shukla, J.; Chattopadhyay, A.; Adarsh, M.B.; Sharma, V.; Vatsa, R.; Rana, N.; Kaur, G.; et al. Prospective Comparison of Angiogenesis-Specific 68Ga-RGD2 PET/CT Imaging Parameters and DAS28-ESR in Rheumatoid Arthritis. *Clin. Nucl. Med.* **2021**, *46*, 556–561. [CrossRef] [PubMed]
49. Morshed, A.; Abbas, A.B.; Hu, J.; Xu, H. Shedding New Light on The Role of $\alpha v\beta 3$ and $\alpha 5\beta 1$ Integrins in Rheumatoid Arthritis. *Molecules* **2019**, *24*, 1537. [CrossRef] [PubMed]
50. Rodrigues Toledo, C.; Tantawy, A.A.; Lima Fuscaldi, L.; Malavolta, L.; de Aguiar Ferreira, C. EGFR- and Integrin $\alpha(V)\beta(3)$-Targeting Peptides as Potential Radiometal-Labeled Radiopharmaceuticals for Cancer Theranostics. *Int. J. Mol. Sci.* **2024**, *25*, 8553. [CrossRef] [PubMed]
51. Khodadust, F.; Steinz, M.M.; Ezdoglian, A.; Philippon, E.M.; Beanio, W.; Windhorst, A.D.; Jansen, G.; Tas, S.W.; van der Laken, C.J. Visualization of Synovial Vascularization In a Preclinical Model of Arthritis Using [^{18}F] Fluciclatide PET/CT: A Novel Integrin-Targeted Molecular Imaging Approach. *Res. Sq.* **2026**. *preprint*. [CrossRef] [PubMed]
52. Kondo, N.; Kato, M.; Oshima, A.; Hirano, F.; Miyazaki, A.; Temma, T. Radioiodinated Bicyclic RGD Peptide Derivatives for Enhanced Tumor Accumulation. *Pharmaceuticals* **2025**, *18*, 549. [CrossRef] [PubMed]
53. Puig-Kröger, A.; Sierra-Filardi, E.; Domínguez-Soto, A.; Samaniego, R.; Corcuera, M.T.; Gómez-Aguado, F.; Ratnam, M.; Sánchez-Mateos, P.; Corbí, A.L. Folate receptor beta is expressed by tumor-associated macrophages and constitutes a marker for M2 anti-inflammatory/regulatory macrophages. *Cancer Res.* **2009**, *69*, 9395–9403. [CrossRef] [PubMed]
54. Varghese, B.; Vlashi, E.; Xia, W.; Ayala Lopez, W.; Paulos, C.M.; Reddy, J.; Xu, L.-C.; Low, P.S. Folate receptor-β in activated macrophages: Ligand binding and receptor recycling kinetics. *Mol. Pharm.* **2014**, *11*, 3609–3616. [CrossRef] [PubMed]
55. Steinz, M.M.; Ezdoglian, A.; Khodadust, F.; Molthoff, C.F.; Srinivasarao, M.; Low, P.S.; Zwezerijnen, G.J.; Yaqub, M.; Beaino, W.; Windhorst, A.D. Folate receptor beta for macrophage imaging in rheumatoid arthritis. *Front. Immunol.* **2022**, *13*, 819163. [CrossRef] [PubMed]
56. Verweij, N.J.F.; Yaqub, M.; Bruijnen, S.T.G.; Pieplenbosch, S.; Ter Wee, M.M.; Jansen, G.; Chen, Q.; Low, P.S.; Windhorst, A.D.; Lammertsma, A.A.; et al. First in man study of [(18)F]fluoro-PEG-folate PET: A novel macrophage imaging technique to visualize rheumatoid arthritis. *Sci. Rep.* **2020**, *10*, 1047. [CrossRef] [PubMed]
57. Moisio, O.; Palani, S.; Virta, J.; Elo, P.; Liljenbäck, H.; Tolvanen, T.; Käkelä, M.; Miner, M.G.; Herre, E.A.; Marjamäki, P.; et al. Radiosynthesis and preclinical evaluation of [(68)Ga]Ga-NOTA-folate for PET imaging of folate receptor β-positive macrophages. *Sci. Rep.* **2020**, *10*, 13593. [CrossRef] [PubMed]
58. Low, P.S.; Henne, W.A.; Doorneweerd, D.D. Discovery and development of folic-acid-based receptor targeting for imaging and therapy of cancer and inflammatory diseases. *Acc. Chem. Res.* **2008**, *41*, 120–129. [CrossRef] [PubMed]
59. Müller, C.; Schibli, R. Folic acid conjugates for nuclear imaging of folate receptor-positive cancer. *J. Nucl. Med.* **2011**, *52*, 1–4. [CrossRef] [PubMed]
60. Matteson, E.L.; Lowe, V.J.; Prendergast, F.G.; Crowson, C.S.; Moder, K.G.; Morgenstern, D.E.; Messmann, R.A.; Low, P.S. Assessment of disease activity in rheumatoid arthritis using a novel folate targeted radiopharmaceutical Folatescan. *Clin. Exp. Rheumatol.* **2009**, *27*, 253–259. [PubMed]
61. Salerno, S.; Viviano, M.; Baglini, E.; Poggetti, V.; Giorgini, D.; Castagnoli, J.; Barresi, E.; Castellano, S.; Da Settimo, F.; Taliani, S. TSPO Radioligands for Neuroinflammation: An Overview. *Molecules* **2024**, *29*, 4212. [CrossRef] [PubMed]
62. Xia, Y.; Ledwitch, K.; Kuenze, G.; Duran, A.; Li, J.; Sanders, C.R.; Manning, C.; Meiler, J. A unified structural model of the mammalian translocator protein (TSPO). *J. Biomol. NMR* **2019**, *73*, 347–364. [CrossRef] [PubMed]
63. Luu, T.G.; Kim, H.K. ^{18}F-Radiolabeled Translocator Protein (TSPO) PET Tracers: Recent Development of TSPO Radioligands and Their Application to PET Study. *Pharmaceutics* **2022**, *14*, 2545. [CrossRef] [PubMed]
64. Wimberley, C.; Lavisse, S.; Hillmer, A.; Hinz, R.; Turkheimer, F.; Zanotti-Fregonara, P. Kinetic modeling and parameter estimation of TSPO PET imaging in the human brain. *Eur. J. Nucl. Med. Mol. Imaging* **2021**, *49*, 246–256. [CrossRef] [PubMed]
65. Bruijnen, S.; Verweij, N.; Gent, Y.; Huisman, M.; Windhorst, A.; Kassiou, M.; van de Ven, P.; Lammertsma, A.; Hoekstra, O.; Voskuyl, A. Imaging disease activity of rheumatoid arthritis by macrophage targeting using second generation translocator protein positron emission tomography tracers. *PLoS ONE* **2019**, *14*, e0222844. [CrossRef] [PubMed]
66. De Groot, M.; Patel, N.; Manavaki, R.; Janiczek, R.L.; Bergstrom, M.; Östör, A.; Gerlag, D.; Roberts, A.; Graves, M.J.; Karkera, Y. Quantifying disease activity in rheumatoid arthritis with the TSPO PET ligand 18F-GE-180 and comparison with 18F-FDG and DCE-MRI. *EJNMMI Res.* **2019**, *9*, 113. [CrossRef] [PubMed]
67. Owen, D.R.; Yeo, A.J.; Gunn, R.N.; Song, K.; Wadsworth, G.; Lewis, A.; Rhodes, C.; Pulford, D.J.; Bennacef, I.; Parker, C.A. An 18-kDa translocator protein (TSPO) polymorphism explains differences in binding affinity of the PET radioligand PBR28. *J. Cereb. Blood Flow Metab.* **2012**, *32*, 1–5. [CrossRef] [PubMed]

68. Singh, P.; Adhikari, A.; Singh, D.; Gond, C.; Tiwari, A.K. The 18-kDa translocator protein PET tracers as a diagnostic marker for neuroinflammation: Development and current standing. *ACS Omega* **2022**, *7*, 14412. [CrossRef] [PubMed]
69. Kreisl, W.C.; Fujita, M.; Fujimura, Y.; Kimura, N.; Jenko, K.J.; Kannan, P.; Hong, J.; Morse, C.L.; Zoghbi, S.S.; Gladding, R.L.; et al. Comparison of [11C]-(R)-PK 11195 and [11C]PBR28, two radioligands for translocator protein (18 kDa) in human and monkey: Implications for positron emission tomographic imaging of this inflammation biomarker. *NeuroImage* **2010**, *49*, 2924–2932. [CrossRef] [PubMed]
70. van Binsbergen, W.H.-J.; de Jongh, J.; Yaqub, M.; van der Pas, S.; van Schaardenburg, D.; Voskuyl, A.E.; Zwezerijnen, G.J.; van der Laken, C.J. Macrophage-Targeted [11C]DPA-713 PET/CT Imaging for Early Therapeutic Evaluation of Anti-Tumor Necrosis Factor Treatment in Rheumatoid Arthritis. *J. Nucl. Med.* **2026**, *67*, 456–462. [CrossRef] [PubMed]
71. Mattner, F.; Katsifis, A.; Bourdier, T.; Loc'h, C.; Berghofer, P.; Fookes, C.; Hung, T.-T.; Jackson, T.; Henderson, D.; Pham, T. Synthesis and pharmacological evaluation of [18F] PBR316: A novel PET ligand targeting the translocator protein 18 kDa (TSPO) with low binding sensitivity to human single nucleotide polymorphism rs6971. *RSC Med. Chem.* **2021**, *12*, 1207–1221. [CrossRef] [PubMed]
72. Singh, S.B.; Bhandari, S.; Bhandari, S.; Bhandari, S.; Singh, R.; Raynor, W.Y.; Hess, S.; Werner, T.J.; Alavi, A.; Revheim, M.-E. Role of PET/CT in diagnosing and monitoring disease activity in rheumatoid arthritis: A review. *Ann. Nucl. Med.* **2024**, *38*, 165–175. [CrossRef] [PubMed]
73. Singh, P.; Singh, V.K.; Gond, C.; Singh, D.; Tiwari, A.K. Current advances in the structure–activity relationship (SAR) analysis of the old/new 18-kDa translocator protein ligands. *Mol. Divers.* **2025**, *29*, 2639–2689. [CrossRef] [PubMed]
74. Lee, S.H.; Denora, N.; Laquintana, V.; Mangiatordi, G.F.; Lopedota, A.; Lopalco, A.; Cutrignelli, A.; Franco, M.; Delre, P.; Song, I.H.; et al. Radiosynthesis and characterization of [18F]BS224: A next-generation TSPO PET ligand insensitive to the rs6971 polymorphism. *Eur. J. Nucl. Med. Mol. Imaging* **2021**, *49*, 110–124. [CrossRef] [PubMed]
75. Rosenkilde, M.M.; Gerlach, L.-O.; Jakobsen, J.S.; Skerlj, R.T.; Bridger, G.J.; Schwartz, T.W. Molecular mechanism of AMD3100 antagonism in the CXCR4 receptor: Transfer of binding site to the CXCR3 receptor. *J. Biol. Chem.* **2004**, *279*, 3033–3041. [PubMed]
76. Pawnikar, S.; Miao, Y. Mechanism of Peptide Agonist Binding in CXCR4 Chemokine Receptor. *Front. Mol. Biosci.* **2022**, *9*, 821055. [CrossRef] [PubMed]
77. De Clercq, E. AMD3100/CXCR4 Inhibitor. *Front. Immunol.* **2015**, *6*, 276. [CrossRef] [PubMed]
78. Yu, J.; Zhou, X.; Shen, L. CXCR4-targeted radiopharmaceuticals for the imaging and therapy of malignant tumors. *Molecules* **2023**, *28*, 4707. [CrossRef] [PubMed]
79. Buck, A.K.; Haug, A.; Dreher, N.; Lambertini, A.; Higuchi, T.; Lapa, C.; Weich, A.; Pomper, M.G.; Wester, H.-J.; Zehndner, A. Imaging of CXC motif chemokine receptor 4 expression in 690 patients with solid or hematologic neoplasms using 68Ga-pentixafor PET. *J. Nucl. Med.* **2022**, *63*, 1687–1692. [CrossRef] [PubMed]
80. Han, Y.; Cao, S.; Liu, J.; Ding, B.; Wang, S.; Pan, J.; Ge, Y.; Cheng, K.; Wang, L.; Ge, L. CXCR4-targeted PET imaging in rheumatoid arthritis: A novel approach for monitoring disease activity and therapeutic response. *EJNMMI Res.* **2025**, *15*, 10. [CrossRef] [PubMed]
81. Wester, H.J.; Keller, U.; Schottelius, M.; Beer, A.; Philipp-Abbrederis, K.; Hoffmann, F.; Šimeček, J.; Gerngross, C.; Lassmann, M.; Herrmann, K. Disclosing the CXCR4 expression in lymphoproliferative diseases by targeted molecular imaging. *Theranostics* **2015**, *5*, 618. [CrossRef] [PubMed]
82. Lapa, C.; Lückerath, K.; Kleinlein, I.; Monoranu, C.M.; Linsenmann, T.; Kessler, A.F.; Rudelius, M.; Kropf, S.; Buck, A.K.; Ernestus, R.-I. 68Ga-pentixafor-PET/CT for imaging of chemokine receptor 4 expression in glioblastoma. *Theranostics* **2016**, *6*, 428. [CrossRef] [PubMed]
83. Herrmann, K.; Schottelius, M.; Lapa, C.; Osl, T.; Poschenrieder, A.; Hänscheid, H.; Lückerath, K.; Schreder, M.; Bluemel, C.; Knott, M. First-in-human experience of CXCR4-directed endoradiotherapy with 177Lu-and 90Y-labeled pentixather in advanced-stage multiple myeloma with extensive intra-and extramedullary disease. *J. Nucl. Med.* **2016**, *57*, 248–251. [CrossRef] [PubMed]
84. Gourni, E.; Demmer, O.; Schottelius, M.; D'Alessandria, C.; Schulz, S.; Dijkgraaf, I.; Schumacher, U.; Schwaiger, M.; Kessler, H.; Wester, H.-J. PET of CXCR4 expression by a 68Ga-labeled highly specific targeted contrast agent. *J. Nucl. Med.* **2011**, *52*, 1803–1810. [CrossRef] [PubMed]
85. Chen, Z.; Xue, Q.; Yao, S. Nuclear medicine application of pentixafor/pentixather targeting CXCR4 for imaging and therapy in related disease. *Mini Rev. Med. Chem.* **2023**, *23*, 787–803. [CrossRef] [PubMed]
86. Poschenrieder, A.; Schottelius, M.; Schwaiger, M.; Wester, H.-J. Preclinical evaluation of [68Ga] NOTA-pentixafor for PET imaging of CXCR4 expression in vivo—A comparison to [68Ga] pentixafor. *EJNMMI Res.* **2016**, *6*, 70. [PubMed]
87. Luna-Gutiérrez, M.; Azorín-Vega, E.; Ocampo-García, B.; Jiménez-Mancilla, N.; Santos-Cuevas, C.; Lara-Almazán, N.; Herrera-García, C.; Meléndez-Alafort, L.; Ferro-Flores, G. Copper-64: An Optimal Radionuclide for the Routine Preparation of PET Imaging Radiotracers from GMP-Lyophilized Gelatin-NOTA-Peptide Kits. *Inorganics* **2026**, *14*, 146. [CrossRef]

88. Carter, L.M.; Ocampo Ramos, J.C.; Olguin, E.A.; Brown, J.L.; Lafontaine, D.; Jokisch, D.W.; Bolch, W.E.; Kesner, A.L. MIRD pamphlet no. 28, part 2: Comparative evaluation of MIRDcalc dosimetry software across a compendium of diagnostic radiopharmaceuticals. *J. Nucl. Med.* **2023**, *64*, 1295–1303. [CrossRef] [PubMed]
89. McConathy, J.; Koshkin, V.S.; Menda, Y.; Rodon, J.; Goenka, A.H.; Moy, R.H.; Morse, S.; Demange, A.; Blumenstein, L.; Babaoglan, B. Targeting fibroblast activation protein with [177Lu] Lu-FAP-2286 in patients with advanced solid tumors in the phase I LuMIERE trial. *Clin. Cancer Res.* **2026**, *32*, 3757–3767. [CrossRef] [PubMed]
90. Fu, H.; Huang, J.; Zhao, L.; Chen, Y.; Xu, W.; Cai, J.; Yu, L.; Pang, Y.; Guo, W.; Su, B.; et al. 177Lu-LNC1004 Radioligand Therapy in Patients with End-stage Metastatic Cancers: A Single-Center, Single-Arm, Phase II Study. *Clin. Cancer Res.* **2025**, *31*, 1415–1426. [CrossRef] [PubMed]
91. Knut, L. Radiosynovectomy in the therapeutic management of arthritis. *World J. Nucl. Med.* **2015**, *14*, 10–15. [CrossRef] [PubMed]
92. van der Zant, F.M.; Boer, R.O.; Moolenburgh, J.D.; Jahangier, Z.N.; Bijlsma, J.W.; Jacobs, J.W. Radiation synovectomy with (90)Yttrium, (186)Rhenium and (169)Erbium: A systematic literature review with meta-analyses. *Clin. Exp. Rheumatol.* **2009**, *27*, 130–139. [PubMed]
93. Kampen, W.U.; Boddenberg-Pätzold, B.; Fischer, M.; Gabriel, M.; Klett, R.; Konijnenberg, M.; Kresnik, E.; Lellouche, H.; Paycha, F.; Terslev, L.; et al. The EANM guideline for radiosynoviorthesis. *Eur. J. Nucl. Med. Mol. Imaging* **2022**, *49*, 681–708. [CrossRef] [PubMed]
94. George, S.C.; Samuel, E.J.J. Developments in (177)Lu-based radiopharmaceutical therapy and dosimetry. *Front. Chem.* **2023**, *11*, 1218670, Corrigendum in *Front. Chem.* **2024**, *12*, 1410803. https://doi.org/10.3389/fchem.2024.1410803. [CrossRef] [PubMed]
95. Vosoughi, S.; Jalilian, A.R.; Shirvani-Arani, S.; Bahrami-Samani, A.; Salek, N. Preparation of 166Dy/166Ho-chitosan as an in vivo generator for radiosynovectomy. *J. Radioanal. Nucl. Chem.* **2017**, *311*, 1657–1664. [CrossRef]
96. Calegaro, J.M.; de Podestá Haje, D.; Machado, J.; Sayago, M.; de Landa, D. Synovectomy using samarium-153 hydroxyapatite in the elbows and ankles of patients with hemophilic arthropathy. *World J. Nucl. Med.* **2018**, *17*, 6–11. [CrossRef] [PubMed]
97. Hao, M.; Zhu, Y.; Su, Z.; Liu, X. Theranostic Nanoprobes for Rheumatoid Arthritis: From Inflammation Visualization to Guided Precision Therapy. *Int. J. Nanomed.* **2026**, *21*, 620949. [CrossRef] [PubMed]
98. Bidkar, A.P.; Zerefa, L.; Yadav, S.; VanBrocklin, H.F.; Flavell, R.R. Actinium-225 targeted alpha particle therapy for prostate cancer. *Theranostics* **2024**, *14*, 2969. [CrossRef] [PubMed]
99. Jalloul, W.; Ghizdovat, V.; Stolniceanu, C.R.; Ionescu, T.; Grierosu, I.C.; Pavaleanu, I.; Moscalu, M.; Stefanescu, C. Targeted alpha therapy: All we need to know about 225Ac's physical characteristics and production as a potential theranostic radionuclide. *Pharmaceuticals* **2023**, *16*, 1679. [CrossRef] [PubMed]
100. Jang, A.; Kendi, A.T.; Johnson, G.B.; Halfdanarson, T.R.; Sartor, O. Targeted alpha-particle therapy: A review of current trials. *Int. J. Mol. Sci.* **2023**, *24*, 11626. [CrossRef] [PubMed]
101. Sjögreen Gleisner, K.; Chouin, N.; Gabina, P.M.; Cicone, F.; Gnesin, S.; Stokke, C.; Konijnenberg, M.; Cremonesi, M.; Verburg, F.A.; Bernhardt, P. EANM dosimetry committee recommendations for dosimetry of 177Lu-labelled somatostatin-receptor-and PSMA-targeting ligands. *Eur. J. Nucl. Med. Mol. Imaging* **2022**, *49*, 1778–1809. [CrossRef] [PubMed]
102. O'Donoghue, J.; Zanzonico, P.; Humm, J.; Kesner, A. Dosimetry in radiopharmaceutical therapy. *J. Nucl. Med.* **2022**, *63*, 1467–1474. [CrossRef] [PubMed]
103. Wadas, T.J.; Pandya, D.N.; Solingapuram Sai, K.K.; Mintz, A. Molecular targeted α-particle therapy for oncologic applications. *Am. J. Roentgenol.* **2014**, *203*, 253–260. [CrossRef] [PubMed]
104. Dewaraja, Y.; Sjögreen-Gleisner, K. *Dosimetry for Radiopharmaceutical Therapy*; International Atomic Energy Agency: Wien, Austria, 2024.
105. Sgouros, G.; Bodei, L.; McDevitt, M.R.; Nedrow, J.R. Radiopharmaceutical therapy in cancer: Clinical advances and challenges. *Nat. Rev. Drug Discov.* **2020**, *19*, 589–608. Erratum in *Nat. Rev. Drug Discov.* **2020**, *19*, 819. https://doi.org/10.1038/s41573-020-0085-5. [CrossRef] [PubMed]
106. Thiele, N.A.; Brown, V.; Kelly, J.M.; Amor-Coarasa, A.; Jermilova, U.; MacMillan, S.N.; Nikolopoulou, A.; Ponnala, S.; Ramogida, C.F.; Robertson, A.K. An eighteen-membered macrocyclic ligand for actinium-225 targeted alpha therapy. *Angew. Chem. Int. Ed.* **2017**, *56*, 14712–14717. [CrossRef] [PubMed]
107. Robertson, A.K.; Ramogida, C.F.; Schaffer, P.; Radchenko, V. Development of 225Ac radiopharmaceuticals: TRIUMF perspectives and experiences. *Curr. Radiopharm.* **2018**, *11*, 156–172. [CrossRef] [PubMed]
108. Bolch, W.E.; Eckerman, K.F.; Sgouros, G.; Thomas, S.R. MIRD pamphlet no. 21: A generalized schema for radiopharmaceutical dosimetry—Standardization of nomenclature. *J. Nucl. Med.* **2009**, *50*, 477–484. [CrossRef] [PubMed]
109. Kratochwil, C.; Haberkorn, U.; Giesel, F.L. 225Ac-PSMA-617 for Therapy of Prostate Cancer. *Semin. Nucl. Med.* **2020**, *50*, 133–140. [CrossRef] [PubMed]
110. Sgouros, G.; Bolch, W.E.; Chiti, A.; Dewaraja, Y.K.; Emfietzoglou, D.; Hobbs, R.F.; Konijnenberg, M.; Sjögreen-Gleisner, K.; Strigari, L.; Yen, T.-C.; et al. ICRU REPORT 96, Dosimetry-Guided Radiopharmaceutical Therapy. *J. ICRU* **2021**, *21*, 1–212. [CrossRef]

111. Sgouros, G.; Roeske, J.C.; McDevitt, M.R.; Palm, S.; Allen, B.J.; Fisher, D.R.; Brill, A.B.; Song, H.; Howell, R.W.; Akabani, G.; et al. MIRD Pamphlet No. 22 (abridged): Radiobiology and dosimetry of alpha-particle emitters for targeted radionuclide therapy. *J. Nucl. Med.* **2010**, *51*, 311–328. [CrossRef] [PubMed]
112. McConathy, J.; Dhawan, M.; Goenka, A.; Moy, R.; Menda, Y.; Chasen, B.; Khushman, M.d.; Mintz, A.; Zakharia, Y.; Sunderland, J.; et al. 177Lu-FAP-2286 in patients with advanced or metastatic solid tumors: Initial data from a phase 1/2 study investigating safety, pharmacokinetics, dosimetry, and preliminary antitumor activity (LuMIERE). *J. Nucl. Med.* **2022**, *63*, 2271.
113. Mourtada, F.; Tomiyoshi, K.; Sims-Mourtada, J.; Mukai-Sasaki, Y.; Yagihashi, T.; Namiki, Y.; Murai, T.; Yang, D.J.; Inoue, T. Actinium-225 Targeted Agents: Where Are We Now? *Brachytherapy* **2023**, *22*, 697–708. [CrossRef] [PubMed]
114. Wang, Y.; Spencer, B.A.; Schmall, J.; Li, E.; Badawi, R.D.; Jones, T.; Cherry, S.R.; Wang, G. High-temporal-resolution lung kinetic modeling using total-body dynamic PET with time-delay and dispersion corrections. *J. Nucl. Med.* **2023**, *64*, 1154–1161. [CrossRef] [PubMed]
115. Zanzonico, P. The MIRD Schema for Radiopharmaceutical Dosimetry: A Review. *J. Nucl. Med. Technol.* **2024**, *52*, 74–85. [CrossRef] [PubMed]
116. Kesner, A.L.; Carter, L.M.; Ramos, J.C.O.; Lafontaine, D.; Olguin, E.A.; Brown, J.L.; President, B.; Jokisch, D.W.; Fisher, D.R.; Bolch, W.E. MIRD pamphlet no. 28, part 1: MIRDcalc—A software tool for medical internal radiation dosimetry. *J. Nucl. Med.* **2023**, *64*, 1117–1124. [CrossRef] [PubMed]
117. Chen, R.; Yang, X.; Ng, Y.L.; Yu, X.; Huo, Y.; Xiao, X.; Zhang, C.; Chen, Y.; Zheng, C.; Li, L. First total-body kinetic modeling and parametric imaging of dynamic 68Ga-FAPI-04 PET in pancreatic and gastric cancer. *J. Nucl. Med.* **2023**, *64*, 960–967. [CrossRef] [PubMed]
118. Yaqub, M.; Verweij, N.J.; Pieplenbosch, S.; Boellaard, R.; Lammertsma, A.A.; Van Der Laken, C.J. Quantitative assessment of arthritis activity in rheumatoid arthritis patients using [11C] DPA-713 positron emission tomography. *Int. J. Mol. Sci.* **2020**, *21*, 3137. [CrossRef] [PubMed]
119. Zhang, X.; Xiong, Z.; Wu, Y.; Cai, W.; Tseng, J.R.; Gambhir, S.S.; Chen, X. Quantitative PET imaging of tumor integrin alphavbeta3 expression with 18F-FRGD2. *J. Nucl. Med.* **2006**, *47*, 113–121. [PubMed]
120. Liolios, C.; Sachpekidis, C.; Kolocouris, A.; Dimitrakopoulou-Strauss, A.; Bouziotis, P. PET diagnostic molecules utilizing multimeric cyclic RGD peptide analogs for imaging integrin αvβ3 receptors. *Molecules* **2021**, *26*, 1792. [CrossRef] [PubMed]
121. Chandrupatla, D.M.; Molthoff, C.F.; Lammertsma, A.A.; van der Laken, C.J.; Jansen, G. The folate receptor β as a macrophage-mediated imaging and therapeutic target in rheumatoid arthritis. *Drug Deliv. Transl. Res.* **2019**, *9*, 366–378. [CrossRef] [PubMed]
122. Brelot, A.; Heveker, N.; Montes, M.; Alizon, M. Identification of residues of CXCR4 critical for human immunodeficiency virus coreceptor and chemokine receptor activities. *J. Biol. Chem.* **2000**, *275*, 23736–23744. [CrossRef] [PubMed]
123. Tian, C.; Mou, L.; Xu, T.; Zheng, W.; Chen, Y. Efficacy of 177 Lu-FAP-2286 and 225 Ac-FAP-2286 in Treating Pancreatic Adenocarcinoma With Lymph Node Metastasis. *Clin. Nucl. Med.* **2026**, *51*, 431–433. [CrossRef] [PubMed]
124. Baum, R.P.; Schuchardt, C.; Singh, A.; Chantadisai, M.; Robiller, F.C.; Zhang, J.; Mueller, D.; Eismant, A.; Almaguel, F.; Zboralski, D.; et al. Feasibility, Biodistribution, and Preliminary Dosimetry in Peptide-Targeted Radionuclide Therapy of Diverse Adenocarcinomas Using (177)Lu-FAP-2286: First-in-Humans Results. *J. Nucl. Med.* **2022**, *63*, 415–423. [CrossRef] [PubMed]
125. Hänscheid, H.; Schirbel, A.; Hartrampf, P.; Kraus, S.; Werner, R.A.; Einsele, H.; Wester, H.J.; Lassmann, M.; Kortüm, M.; Buck, A.K. Biokinetics and dosimetry of 177Lu-pentixather. *J. Nucl. Med.* **2022**, *63*, 754–760. [CrossRef] [PubMed]
126. Tu, Y.; Ma, X.; Chen, H.; Fan, Y.; Jiang, L.; Zhang, R.; Cheng, Z. Molecular Imaging of Matrix Metalloproteinase-2 in Atherosclerosis Using a Smart Multifunctional PET/MRI Nanoparticle. *Int. J. Nanomed.* **2022**, *17*, 6773–6789. [CrossRef] [PubMed]
127. Crișan, G.; Moldovean-Cioroianu, N.S.; Timaru, D.-G.; Andrieș, G.; Căinap, C.; Chiș, V. Radiopharmaceuticals for PET and SPECT imaging: A literature review over the last decade. *Int. J. Mol. Sci.* **2022**, *23*, 5023. [CrossRef] [PubMed]

Disclaimer/Publisher's Note: The statements, opinions and data contained in all publications are solely those of the individual author(s) and contributor(s) and not of MDPI and/or the editor(s). MDPI and/or the editor(s) disclaim responsibility for any injury to people or property resulting from any ideas, methods, instructions or products referred to in the content.